Geophysical Journal International

Geophys. J. Int. (2013) **192,** 473–499 doi: 10.1093/gji/ggs043

Boundary element solutions for broad-band 3-D geo-electromagnetic problems accelerated by an adaptive multilevel fast multipole method

Zhengyong Ren, Thomas Kalscheuer, Stewart Greenhalgh and Hansruedi Maurer

Institute of Geophysics, Department of Earth Sciences, ETH Zurich, Sonneggstr. 5, 8092 Zurich, Switzerland. E-mail: renzh@aug.ig.erdw.ethz.ch

Accepted 2012 October 22. Received 2012 October 22; in original form 2011 November 4

SUMMARY

We have developed a generalized and stable surface integral formula for 3-D uniform inducing field and plane wave electromagnetic induction problems, which works reliably over a wide frequency range. Vector surface electric currents and magnetic currents, scalar surface electric charges and magnetic charges are treated as the variables. This surface integral formula is successfully applied to compute the electromagnetic responses of 3-D topography to low frequency magnetotelluric and high frequency radio-magnetotelluric fields. The standard boundary element method which is used to solve this surface integral formula quickly exceeds the memory capacity of modern computers for problems involving hundreds of thousands of unknowns. To make the surface integral formulation applicable and capable of dealing with large-scale 3-D geo-electromagnetic problems, we have developed a matrix-free adaptive multilevel fast multipole boundary element solver. By means of the fast multipole approach, the time-complexity of solving the final system of linear equations is reduced to $O(m \log m)$ and the memory cost is reduced to $O(m)$, where m is the number of unknowns. The analytical solutions for a half-space model were used to verify our numerical solutions over the frequency range 0.001–300 kHz. In addition, our numerical solution shows excellent agreement with a published numerical solution for an edge-based finite-element method on a trapezoidal hill model at a frequency of 2 Hz. Then, a high frequency simulation for a similar trapezoidal hill model was used to study the effects of displacement currents in the radio-magnetotelluric frequency range. Finally, the newly developed algorithm was applied to study the effect of moderate topography and to evaluate the applicability of a 2-D RMT inversion code that assumes a flat air–Earth interface, on RMT field data collected at Smørgrav, southern Norway. This paper constitutes the first part of a hybrid boundary element-finite element approach to compute the electromagnetic field inside structures involving complex 3-D conductivity and permittivity distributions.

Key words: Numerical solutions; Electromagnetic theory; Magnetotelluric; Magnetic and electrical properties.

INTRODUCTION

Plane wave geo-electromagnetic induction methods such as the magnetotelluric (MT; Berdichevsky & Dmitriev 2008) and the radio-magnetotelluric (RMT) methods (Pedersen *et al.* 2006) are widely used in geophysical exploration. At low frequencies, conduction currents dominate and displacement currents can be neglected. This forms the basis for the quasi-static approximation which underlies the MT method for studying the deep structure of the Earth. At much higher frequencies, in the RMT range (10–300 kHz), and on terrain with resistivities above a few thousand Ohm metres, displacement currents are comparable or even larger than conduction currents and ought to be taken into account. In such cases, neglecting displacement currents will decrease the reliability of inverted RMT models (Kalscheuer *et al.* 2008). In areas with resistivities below a couple of thousand Ohm metres, the quasi-static approximation is rightfully made in the inversion of RMT data. In recent years, the RMT method, in combination with the direct current resistivity method (Candansayar & Tezkan 2008; Kalscheuer *et al.* 2010) and controlled-source electromagnetic methods (Pedersen *et al.* 2005), has become more and more important in imaging shallow subsurface structure, such as in fracture zone detection (Pedersen & Engels 2005; Ismail & Pedersen 2011), monitoring active faults (Candansayar & Tezkan 2008), hydrogeological surveying (Pedersen *et al.* 2005; Seher & Tezkan 2007), and environmental/engineering investigations (Tezkan *et al.* 1996, 2005; Tezkan & Saraev 2008). Therefore, to assure correct modelling results in resistive environments it is important to have

available a broad-band geo-electromagnetic solver, which cannot only deal with low frequency MT problems, but is also suitable for high frequency RMT problems.

There are basically four candidate numerical simulation techniques to choose from for computing 3-D electromagnetic responses, namely finite-difference methods (FDM), finite-element methods (FEM), volume integral equation methods (IE) and surface integral equation methods. The FDM (Mackie *et al.* 1994; Aprea *et al.* 1997; Haber *et al.* 2000; Newman & Alumbaugh 2002; Hou *et al.* 2006) is very suitable for fast modelling of electromagnetic fields on geometrically simple models. However, it is less convenient when treating resistivity models that involve complicated shapes and curved interfaces such as free surface topography. This disadvantage of the FDM can be overcome with the FEM (Badea *et al.* 2001; Mitsuhata & Uchida 2004; Nam *et al.* 2007), which is capable of solving complicated geometrical problems by utilizing unstructured meshes (Key & Weiss 2006; Franke *et al.* 2007; Li & Key 2007; Mukherjee & Everett 2011). Due to the nature of the geo-electromagnetic problem, additional unknowns have to be introduced to discretize the air domain above the ground for both the FDM and the FEM. To avoid discretizing the air domain and to keep the number of unknowns to a minimum, we can look to the volume and surface integral equation methods. The success of volume integral equation methods is strongly dependent on having an accurate solution for the Green's functions in the background medium. In simple cases, such as layered earth models, for which the Green's functions are readily available, the volume integral method might be the best choice (Hohmann 1975; Weidelt 1975; Avdeev *et al.* 2002). However, if the background medium is reasonably complex, then no analytic Green's functions exist, and several anomalous computation domains need to be discretized. This leads to large dense matrices and iterative solving procedures, which might produce inaccurate results (Zhdanov *et al.* 2006). Unlike the volume integral methods, the surface integrals methods (boundary element methods, BEM) use the full space Green's functions which can generally be expressed in simple closed-form (Colton & Kress 1983).

The main disadvantage of the surface integral approach though is its inability to handle models having complicated distributions of subsurface electrical parameters. Therefore we propose to use it only as the first part of a hybrid approach to deal with complex models. The arbitrary surface topography is handled by the surface integral approach while the other part of the modelling (to handle the subsurface structure) will be done with a finite element approach. Careful treatment is required to derive numerically stable surface integral formulations, due to the well-known low frequency and internal resonance problems (Colton & Kress 1983; Liu & Lamontagne 1998; Jin 2002) for 3-D electromagnetic problems. The surface integral methods contain weak, strong or even hyper singular integrals which need to be evaluated. The complexity of correctly computing these singular integrals sometimes exceeds the difficulty of formulating the surface integral equations themselves. As a consequence, surface integral approaches have not been very popular in geo-electromagnetic investigations (Parry & Ward 1971; Doherty 1988; Liu & Becker 1992; Xu *et al.* 1997; Liu & Lamontagne 1998). However, the inherent advantage of surface integral approaches of being able to reduce a 3-D problem to a 2-D problem prompts us to explore its potential power in geo-electromagnetic modelling. Inspired by the work of Weidelt (1975), and to avoid the necessity to discretize the air domain and at the same time to deal with arbitrary surface topography (air–Earth interface), the surface integral equation approach is the method of choice for complicated 3-D topography, which we further develop in this paper.

The surface integral equation method can be formulated in terms of the direct physical electromagnetic fields (Parry & Ward 1971; Doherty 1988; Xu *et al.* 1997; Liu & Lamontagne 1998), the indirect electric and magnetic potentials (Tsuboi & Misaki 1987; Ahmed *et al.* 1988; Rucker *et al.* 1995), or virtual equivalent currents and charges (Mayergoyz 1982; Liu & Becker 1992; Harrington 1993; Zheng 1997; Homentcovschi 2002). The disadvantages of indirect surface integral approaches using vector and scalar potential functions are twofold. First, the electromagnetic fields have to be computed from the potentials in terms of extra gradient and/or curl operations so that higher order shape functions and denser meshes than in a direct solution for electromagnetic field components are required to achieve suitable accuracy. Second, the continuity conditions at boundary surfaces which enforce the uniqueness of solutions, have to be applied in a nontrivial way, especially for multiply connected regions of different electrical properties, due to the multivalued nature of the potentials at the interfaces (Pérez-Gavilán & Aliabadi 2001; Pusch & Ostrowski 2010). By contrast, both the direct surface integral equation approaches which treat the physical electromagnetic fields as the variables and the virtual surface approaches allow lower order shape functions and coarse meshes to be used. Furthermore, more physically meaningful explanations of induced or scattered electromagnetic fields in the bodies can be made in terms of the virtual currents and charges on surfaces enclosing the bodies. Unlike high frequency antenna design and wave propagation simulation, in which the scattered electromagnetic fields can be stably expressed by surface magnetic currents and electric currents, the bridge or link between surface currents and charges is broken for low frequency geo-electromagnetic problems from the numerical point of view. Recently, the importance of introducing surface charges and surface currents as variables to solve high frequency scattering by dielectric objects was investigated by Taskinen & Ylä-Oijala (2006). It was found that both surface currents and charges are needed to guarantee the stability of numerical solutions.

In this study, we present a novel and numerically stable surface integral formula in terms of equivalent surface magnetic currents, surface electric currents and surface magnetic and electric charges, to solve the geo-electromagnetic induction problem. The new scheme offers the following advantages: (1) stable numerical results can be obtained for both high frequency and low frequency problems; (2) the condition number of the final discretized system of linear equations is well behaved and (3) with the help of the vector Green's theorem, boundary conditions on internal interfaces can be enforced in a trivial way such that the equations for multiply connected regions can be solved naturally. Although this new surface integral formula is stable for broad-band electromagnetic problems, there is a $O(m^2)$ time complexity of assembling the final linear system of equations, and a $O(m^2)$ and $O(m^3)$ cost for storing and solving, respectively, this linear system of equations by direct solvers. Here, m is the number of unknowns. This imposes a serious limitation on its applicability to practical large-scale geo-electromagnetic

problems. To accelerate assembling and solving the entire system of linear equations, an optimal matrix-free adaptive multilevel fast multipole AMFM) method is developed. Compared with other potentially accelerating algorithms which are only suitable for uniform grids, such as adaptive integral methods (Bleszynski *et al.* 1996), fast Fourier transform methods (Borup & Gandhi 1984) and the standard fast multipole method (Liu 2009), the matrix-free AMFM algorithm presented in this study can also work on non-uniform grids (Buchau *et al.* 2000), which are widely used in geo-electromagnetic problems to reduce the computational cost, with a time complexity $O(m \log m)$ for assembling the system of linear equations and a linear $O(m)$ memory cost for iterative solvers.

To validate the new surface integral formula and the proposed optimal AMFM algorithm, the analytical solutions for a half-space model at frequencies varying from 0.001 Hz to 300 kHz are used. In addition, a trapezoidal hill model at a frequency of 2 Hz is tested to compare our numerical solutions with that from an edge-based 3-D FEM (Nam *et al.* 2007). Finally, using the new code we study the effect of displacement currents on RMT responses in the presence of significant topography for a field example from Smørgrav, southern Norway.

GENERALIZED SURFACE INTEGRAL FORMULA

Single homogeneous isotropic body

Assuming a homogeneous and isotropic medium Ω, in which the conductivity $\sigma(S/m)$, the electric permittivity $\varepsilon(F/m)$ and the magnetic permeability $\mu(H/m)$ are constant, we start with the stable Maxwell equations (Tsuboi & Misaki 1987; Shen 1995; Jin 2002) in terms of $\mathbf{E}$ (electric field strength, V m^{-1}) and $\mathbf{B}$ (magnetic flux density, T) in the frequency domain [assuming a time varying factor $\exp(-\mathrm{i}\omega t)$]

$$\nabla \times \mathbf{E} = \mathrm{i}\omega \mathbf{B}, \tag{1}$$

$$\nabla \times \mathbf{B} = \mu(\sigma - \mathrm{i}\omega\varepsilon)\mathbf{E}, \tag{2}$$

$$\nabla \cdot \mathbf{E} = 0, \tag{3}$$

$$\nabla \cdot \mathbf{B} = 0, \tag{4}$$

where the imaginary unit $\mathrm{i} = \sqrt{-1}$, $\omega = 2\pi f$ is the angular frequency and f is the frequency. Eliminating $\mathbf{B}$ from eq. (1) or $\mathbf{E}$ from eq. (2) , we have

$$\begin{aligned} &\nabla \times \nabla \times \mathbf{E} - k^2\mathbf{E} = \mathbf{0}, \\ &\nabla \times \nabla \times \mathbf{B} - k^2\mathbf{B} = \mathbf{0}. \end{aligned} \tag{5}$$

Here, $k = \sqrt{\mathrm{i}\omega\mu(\sigma - i\omega\varepsilon)} = \sqrt{-\xi\chi}$ is the wavenumber or complex propagation constant, $\xi = -\mathrm{i}\omega\mu$ is the impedivity and $\chi = (\sigma - i\omega\varepsilon)$ is the admittivity.

For an arbitrary vector-scalar pair, $\mathbf{W}$ and φ, having continuous second derivatives over the domain Ω, the following vector-scalar Green's identity holds [Jin (2002), eq. (14.41)]

$$\iiint_{\Omega} \left[\varphi \nabla \times \nabla \times \mathbf{W} + \nabla \cdot \mathbf{W} \nabla\varphi + \nabla^2\varphi\mathbf{W}\right] \mathrm{d}V = \oiint_{\partial\Omega} \left[\varphi\hat{\mathbf{n}} \times \nabla \times \mathbf{W} + (\hat{\mathbf{n}} \cdot \mathbf{W})\nabla\varphi + (\hat{\mathbf{n}} \times \mathbf{W}) \times \nabla\varphi\right] \mathrm{d}s, \tag{6}$$

where $\hat{\mathbf{n}}$ is an outward normal unit vector on the boundary $\partial\Omega$ of Ω. Mathematically, the scalar function $\varphi = \varphi(\mathbf{r})$ could be any function of position $\mathbf{r} \in \Omega$ with at least continuous second derivatives, $\varphi(\mathbf{r}) \in C^n(\Omega)$, $n \geq 2$. Physically, we consider the scalar function $\varphi(\mathbf{r})$ to be the potential generated by a unit source at a point $\acute{\mathbf{r}} \in \Omega$. The potential field will satisfy the inhomogeneous scalar Helmholtz equation

$$\nabla^2\varphi(\mathbf{r}, \acute{\mathbf{r}}) + k^2\varphi(\mathbf{r}, \acute{\mathbf{r}}) = -\delta(\mathbf{r}, \acute{\mathbf{r}}). \tag{7}$$

Without considering boundary conditions, one suitable form for $\varphi(\mathbf{r}, \acute{\mathbf{r}})$ is $\varphi(\mathbf{r}, \acute{\mathbf{r}}) = \frac{\exp(\mathrm{i}k|\mathbf{r}-\acute{\mathbf{r}}|)}{4\pi|\mathbf{r}-\acute{\mathbf{r}}|}$. Substituting this expression for $\varphi(\mathbf{r}, \acute{\mathbf{r}})$ into eq. (6), and letting $\mathbf{W} = \mathbf{E}$ and $\mathbf{W} = \mathbf{B}$, respectively, a pair of surface integral equations for the electric field $\mathbf{E}$ and magnetic field $\mathbf{B}$ is obtained

$$\Theta\mathbf{E}(\acute{\mathbf{r}}) = -\oiint_{\mathbf{r}\in\partial\Omega} \left[\mathrm{i}\omega\varphi\hat{\mathbf{n}} \times \mathbf{B} + (\hat{\mathbf{n}} \cdot \mathbf{E})\nabla\varphi + (\hat{\mathbf{n}} \times \mathbf{E}) \times \nabla\varphi\right] \mathrm{d}s, \tag{8}$$

$$\Theta\mathbf{B}(\acute{\mathbf{r}}) = -\oiint_{\mathbf{r}\in\partial\Omega} \left[\mu(\sigma - \mathrm{i}\omega\varepsilon)\varphi\hat{\mathbf{n}} \times \mathbf{E} + (\hat{\mathbf{n}} \cdot \mathbf{B})\nabla\varphi + (\hat{\mathbf{n}} \times \mathbf{B}) \times \nabla\varphi\right] \mathrm{d}s, \tag{9}$$

where the gradient operator ∇ is on $\mathbf{r} \in \partial\Omega$ and Θ is the solid angle subtended at $\acute{\mathbf{r}}$

$$\Theta = \iiint_{\Omega} \delta(\mathbf{r}, \acute{\mathbf{r}})\, \mathrm{d}V = \begin{cases} 1 & \acute{\mathbf{r}} \in \Omega \\ 1/2 & \acute{\mathbf{r}} \in \partial\Omega. \end{cases}$$

eq. (8) is referred to as the electric field integral equation (EFIE) and eq. (9) is referred to as the magnetic field integral equation (MFIE). In eqs (8) and (9), the normal components of $\mathbf{E}$ and $\mathbf{B}$ can be represented in terms of the tangential components of $\mathbf{B}$ and $\mathbf{E}$, respectively, (Harrington 1993),

$$\hat{\mathbf{n}} \cdot \mathbf{E} = \frac{1}{k^2} \hat{\mathbf{n}} \cdot (\nabla \times \nabla \times \mathbf{E}) = \frac{-1}{\mu\chi} \nabla \cdot (\hat{\mathbf{n}} \times \mathbf{B}),\ \hat{\mathbf{n}} \cdot \mathbf{B} = \frac{\mu}{\xi} \nabla \cdot (\hat{\mathbf{n}} \times \mathbf{E}). \tag{10}$$

This relationship is valid at high frequencies, such as wave propagation fields, and has the benefit of reducing the number of variables which means the normal components of the electric and magnetic fields can be avoided because they can be represented by the tangential components of the magnetic field and electric field, respectively. Such a representation shows that the electromagnetic fields inside a homogeneous and isotropic medium are solely determined by the surface tangential electromagnetic fields. Therefore, the surface distributions of the electromagnetic fields can be viewed as the 'sources' which generate the fields inside the domain. However, there is a risk of numerical instability with this relationship, due to the small values of admittivity and impedivity at low frequency, as in highly resistive bodies such as the air space. As a consequence, to avoid this potential risk, a full set of virtual equivalent surface electric currents $\tilde{\mathbf{J}}$ and charges $\tilde{\beta}$, surface magnetic currents $\tilde{\mathbf{M}}$ and charges $\tilde{\alpha}$ is considered in this study, $\tilde{\mathbf{J}} = \frac{1}{\mu} \hat{\mathbf{n}} \times \mathbf{B}$, $\tilde{\mathbf{M}} = \hat{\mathbf{n}} \times \mathbf{E}$, $\tilde{\beta} = \hat{\mathbf{n}} \cdot \mathbf{B}$, $\tilde{\alpha} = \hat{\mathbf{n}} \cdot \mathbf{E}$. Using the vector identity $\mathbf{W} = (\hat{\mathbf{n}} \times \mathbf{W}) \times \hat{\mathbf{n}} + (\hat{\mathbf{n}} \cdot \mathbf{W})\, \hat{\mathbf{n}}$, and considering the above definitions, we have

$$\Theta \left[\tilde{\mathbf{M}} \times \hat{\mathbf{n}} + \tilde{\alpha}\hat{\mathbf{n}}\right]_{(\acute{\mathbf{r}})} = - \oiint_{\mathbf{r} \in \partial\Omega} \left[-\xi\varphi\tilde{\mathbf{J}} + \tilde{\alpha}\nabla\varphi + \tilde{\mathbf{M}} \times \nabla\varphi\right] \mathrm{d}s, \tag{11}$$

$$\Theta \left[\mu\tilde{\mathbf{J}} \times \hat{\mathbf{n}} + \tilde{\beta}\hat{\mathbf{n}}\right]_{(\acute{\mathbf{r}})} = - \oiint_{\mathbf{r} \in \partial\Omega} \left[\mu\chi\varphi\tilde{\mathbf{M}} + \tilde{\beta}\nabla\varphi + \mu\tilde{\mathbf{J}} \times \nabla\varphi\right] \mathrm{d}s. \tag{12}$$

Two connected bodies

We consider now two arbitrary but dissimilar homogeneous and isotropic media Ω_i with electromagnetic parameters $(\sigma_i, \varepsilon_i, \mu_i)$, $i = 0, 1$, as shown in Fig. 1. For the geo-electromagnetic problem, the subscript 0 represents air and the subscript 1 the Earth. The common surface connecting these two bodies is $\Gamma = \partial\Omega_0 \cap \partial\Omega_1$. The surface of body Ω_0 is $\partial\Omega_0 = \Gamma + \Gamma_0$, where Γ_0 is the part of the surface which only belongs to Ω_0 . The surface of body Ω_1 is $\partial\Omega_1 = \Gamma + \Gamma_1$, where Γ_1 is the part of the surface which only belongs to Ω_1. On Γ_0 and Γ_1, the electromagnetic fields are given as the boundary conditions. The normal vector $\hat{\mathbf{n}}$ on the common surface Γ is defined to point in the direction from Ω_0 to Ω_1. The electromagnetic fields on the common surface Γ are unknown. Following on from eqs (11) and (12), once the electromagnetic fields on the common surface have been determined, the fields at any point inside $\Omega_0 \cup \Omega_1$ can be computed. To obtain stable numerical solutions of surface currents and charges, the full set of boundary conditions should be satisfied simultaneously. This implies

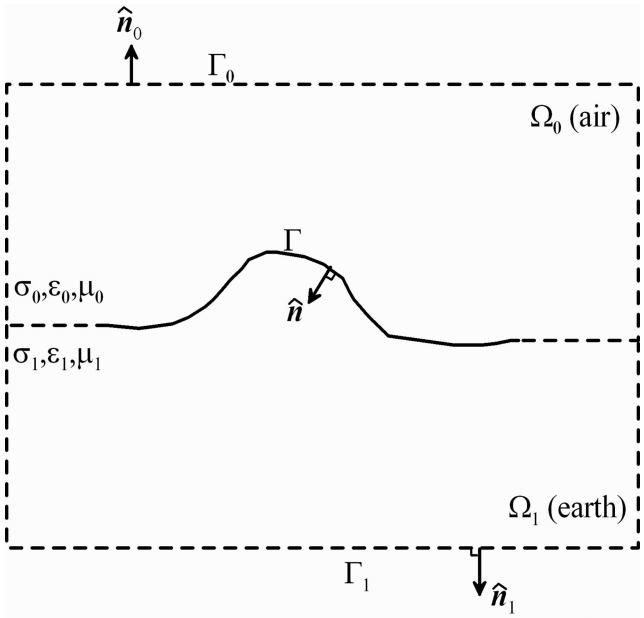

Figure 1. The geometrical configuration of two connected arbitrary bodies Ω_0 and Ω_1. For example, Ω_0 could be the air and Ω_1 the Earth. The conductivity of Ω_0 is required to be less than or equal to that of Ω_1 and $\hat{\mathbf{n}}$, $\hat{\mathbf{n}}_0$ and $\hat{\mathbf{n}}_1$ are unit normal vectors to the three surfaces Γ, Γ_0 and Γ_1.

that both the EFIE of eq. (11) and MFIE of eq. (12) should be used in both Ω_0 and Ω_1. This is a variant of the combined field integral equations (CFIE; Jin 2002; Ylä-Oijala 2008) by which internal resonance problems which cause extremely unstable numeral results at certain frequencies can be avoided.

Applying both the EFIE eq. (11) and the MFIE eq. (12) to both Ω_0 and Ω_1, and letting the observation point $\acute{\mathbf{r}}$ approach the smooth surface Γ, we have

$$\frac{1}{2}\left[\tilde{\mathbf{M}}_0 \times \hat{\mathbf{n}} + \tilde{\alpha}_0 \hat{\mathbf{n}}\right]_{(\acute{\mathbf{r}})} = -\iint_{\mathbf{r}\in\Gamma} \left[-\xi_0\varphi_0\tilde{\mathbf{J}}_0 + \tilde{\alpha}_0\nabla\varphi_0 + \tilde{\mathbf{M}}_0 \times \nabla\varphi_0\right] \mathrm{d}s + \mathbf{E}_{\Gamma_0}(\acute{\mathbf{r}}), \tag{13}$$

$$\frac{1}{2}\left[\mu_0\tilde{\mathbf{J}}_0 \times \hat{\mathbf{n}} + \tilde{\beta}_0 \hat{\mathbf{n}}\right]_{(\acute{\mathbf{r}})} = -\iint_{\mathbf{r}\in\Gamma} \left[\mu_0\chi_0\varphi_0\tilde{\mathbf{M}}_0 + \tilde{\beta}_0\nabla\varphi_0 + \mu_0\tilde{\mathbf{J}}_0 \times \nabla\varphi_0\right] \mathrm{d}s + \mathbf{B}_{\Gamma_0}(\acute{\mathbf{r}}), \tag{14}$$

$$\frac{1}{2}\left[\tilde{\mathbf{M}}_1 \times \hat{\mathbf{n}} + \tilde{\alpha}_1 \hat{\mathbf{n}}\right]_{(\acute{\mathbf{r}})} = \iint_{\mathbf{r}\in\Gamma} \left[-\xi_1\varphi_1\tilde{\mathbf{J}}_1 + \tilde{\alpha}_1\nabla\varphi_1 + \tilde{\mathbf{M}}_1 \times \nabla\varphi_1\right] \mathrm{d}s + \mathbf{E}_{\Gamma_1}(\acute{\mathbf{r}}), \tag{15}$$

$$\frac{1}{2}\left[\mu_1\tilde{\mathbf{J}}_1 \times \hat{\mathbf{n}} + \tilde{\beta}_1 \hat{\mathbf{n}}\right]_{(\acute{\mathbf{r}})} = \iint_{\mathbf{r}\in\Gamma} \left[\mu_1\chi_1\varphi_1\tilde{\mathbf{M}}_1 + \tilde{\beta}_1\nabla\varphi_1 + \mu_1\tilde{\mathbf{J}}_1 \times \nabla\varphi_1\right] \mathrm{d}s + \mathbf{B}_{\Gamma_1}(\acute{\mathbf{r}}), \tag{16}$$

where $\mathbf{E}_{\Gamma_0}(\acute{\mathbf{r}})$ is the electric field contributed by the known electromagnetic fields on Γ_0 to the observation point $\acute{\mathbf{r}}$ defined by eq. (8) and $\mathbf{B}_{\Gamma_0}(\acute{\mathbf{r}})$ is the magnetic field originating from the known electromagnetic fields on Γ_0 defined by eq. (9). $\mathbf{E}_{\Gamma_1}(\acute{\mathbf{r}})$ and $\mathbf{B}_{\Gamma_1}(\acute{\mathbf{r}})$ have similar definitions. On the common surface Γ, these virtual currents and charges are connected by the full set of the following boundary conditions: $\tilde{\mathbf{J}}_0 = \tilde{\mathbf{J}}_1$, $\tilde{\mathbf{M}}_0 = \tilde{\mathbf{M}}_1$, $\tilde{\beta}_0 = \tilde{\beta}_1$, $\chi_0\tilde{\alpha}_0 = \chi_1\tilde{\alpha}_1$. Here, a constraint is assumed for the real parts of admittivities of bodies Ω_0 and Ω_0, viz., $Re(\chi_0) \leq Re(\chi_1)$, so that we can define two well-behaved factors D and Q

$$D = \frac{\chi_0}{\chi_1} \quad \text{where } |D| \ll \infty, \qquad 0 < Q = \frac{\xi_0}{\xi_1} \ll \infty.$$

In terms of the constraint satisfied by body Ω_0, the surface currents and charges for body Ω_0 are taken as variables, that is $\tilde{\mathbf{J}} \equiv \tilde{\mathbf{J}}_0$, $\tilde{\mathbf{M}} \equiv \tilde{\mathbf{M}}_0$, $\tilde{\beta} \equiv \tilde{\beta}_0$, $\tilde{\alpha} \equiv \tilde{\alpha}_0$. Adding the two EFIE eqs (13) and (15), and the two MFIE eqs (14) and (16), respectively, and by further manipulation, we obtain

$$[\tilde{\mathbf{M}} \times \hat{\mathbf{n}} + \frac{1+D}{2}\tilde{\alpha}\hat{\mathbf{n}}]_{(\acute{\mathbf{r}})} = \iint_{\mathbf{r}\in\Gamma} \left[\tilde{\mathbf{M}} \times (\nabla\varphi_1 - \nabla\varphi_0) + \tilde{\mathbf{J}}(-\xi_1\varphi_1 + \xi_0\varphi_0) + \tilde{\alpha}(D\nabla\varphi_1 - \nabla\varphi_0)\right] \mathrm{d}s + \mathbf{E}_{\Gamma_0+\Gamma_1}(\acute{\mathbf{r}}), \tag{17}$$

$$\left[\frac{(-\xi_0 - \xi_1)}{2}\tilde{\mathbf{J}} \times \hat{\mathbf{n}} + \mathrm{i}\omega\tilde{\beta}\hat{\mathbf{n}}\right]_{(\acute{\mathbf{r}})} = \iint_{\mathbf{r}\in\Gamma} \left[\tilde{\mathbf{J}} \times (-\xi_1\nabla\varphi_1 + \xi_0\nabla\varphi_0) + \tilde{\mathbf{M}}\left(k_1^2\varphi_1 - k_0^2\varphi_0\right) + \mathrm{i}\omega\tilde{\beta}(\nabla\varphi_1 - \nabla\varphi_0)\right] \mathrm{d}s + \mathrm{i}\omega\mathbf{B}_{\Gamma_0+\Gamma_1}(\acute{\mathbf{r}}). \tag{18}$$

It should be noted that the coefficients in front of each integrand in eqs (17) and (18) are quite different in amplitude. This would lead to large differences in the entries for the final system of linear equations, and hence, to an ill-conditioned problem. To improve conditioning, a new set of rescaled surface currents and charges (Colton & Kress 1983; Ylä-Oijala & Taskinen 2007) is introduced on the surface Γ

$$\mathbf{J} \equiv \sqrt{-\xi_1}\tilde{\mathbf{J}}, \tag{19}$$

$$\mathbf{M} \equiv \sqrt{\chi_1}\tilde{\mathbf{M}}, \tag{20}$$

$$\beta \equiv \frac{i\omega}{\sqrt{-\xi_1}}\tilde{\beta}, \tag{21}$$

$$\alpha \equiv \sqrt{\chi_1}\tilde{\alpha}. \tag{22}$$

Substituting these rescaled currents and charges into eqs (17) and (18), we obtain the following generalized surface integral formulae for the two connected homogeneous and isotropic media

$$\left(\mathbf{M} \times \hat{\mathbf{n}} + \frac{1+D}{2}\alpha\hat{\mathbf{n}}\right)_{(\acute{\mathbf{r}})} = \iint_{\mathbf{r}\in\Gamma} [\mathbf{M} \times (\nabla\varphi_1 - \nabla\varphi_0) + k_1\mathbf{J}(\varphi_1 - Q\varphi_0) + \alpha(D\nabla\varphi_1 - \nabla\varphi_0)]\,\mathrm{d}s + \sqrt{\chi_1}\mathbf{E}_{\Gamma_0+\Gamma_1}(\acute{\mathbf{r}}), \tag{23}$$

$$\left(\frac{1+Q}{2}\mathbf{J} \times \hat{\mathbf{n}} + \beta\hat{\mathbf{n}}\right)_{(\acute{\mathbf{r}})} = \iint_{\mathbf{r}\in\Gamma} [\mathbf{J} \times (\nabla\varphi_1 - Q\nabla\varphi_0) + k_1\mathbf{M}(\varphi_1 - QD\varphi_0) + \beta(\nabla\varphi_1 - \nabla\varphi_0)]\,\mathrm{d}s + \frac{\mathrm{i}\omega}{\sqrt{-\xi_1}}\mathbf{B}_{\Gamma_0+\Gamma_1}(\acute{\mathbf{r}}). \tag{24}$$

Topographic models

For a typical geo-electromagnetic topographic model, the body Ω_0 is set to be the free space or air and the body Ω_1 represents the Earth. The conductivity of free air is σ_0 , while ε_0 and μ_0 are the electric permittivity and the magnetic permeability values for free space. On Γ_0 and Γ_1, the analytical solutions for a 1-D half-space model with sources polarized in two different directions (E_x and H_x) are enforced. The amplitude of the incident electric (E_x^p) or magnetic (H_x^p) field just above the interface (with coordinate $z = 0$) is arbitrarily set to unit value, depending on which polarization (p) is being considered. Using these boundary conditions, the source terms $\mathbf{E}_{\Gamma_0+\Gamma_1}$ in eq. (23) and $\mathbf{B}_{\Gamma_0+\Gamma_1}$ in eq. (24) are computed. Then, on the common air–Earth surface Γ, the unknown surface currents and charges are solved via eqs (23) and (24).

STANDARD BEM APPROACH

On the common undulating surface Γ, a local coordinate system (u, v, n) is introduced in which $\hat{\mathbf{n}}$ is the normal unit vector to the topographic surface, and $\hat{\mathbf{u}}$ and $\hat{\mathbf{v}}$ are unit vectors in the two tangential directions orthogonal to each other. In this system the tangential vectors $\mathbf{J}$ and $\mathbf{M}$ are defined as

$$\mathbf{M} = M_u\hat{\mathbf{u}} + M_v\hat{\mathbf{v}}, \qquad \mathbf{J} = J_u\hat{\mathbf{u}} + J_v\hat{\mathbf{v}}. \tag{25}$$

To approximate complicated surfaces, a triangulation grid (Shewchuk 1996) is adopted on $\Gamma = \cup\triangle_i$, $i = 1, \ldots, N$, where N is the number of triangles. As no differential operators are applied to the surface currents and charges, zero-order constant shape functions are suitable to represent these surface distributions. In addition, the point collocation method rather than the Galerkin residual method is naturally employed with zero-order constant shape functions; this can dramatically speed up the assembling procedure and at the same time maintain the desired accuracy of the final solution (Jin 2002). Substituting eq. (25) into eqs (23) and (24), and by applying $\hat{\mathbf{u}}(\acute{\mathbf{r}})\cdot$, $\hat{\mathbf{v}}(\acute{\mathbf{r}})\cdot$ and $\hat{\mathbf{n}}(\acute{\mathbf{r}})\cdot$ operators to eqs (23) and (24), the following system of linear equations is obtained

$$\begin{bmatrix} M_u \\ M_v \\ \frac{1+D}{2}\alpha \\ \frac{1+Q}{2}J_u \\ \frac{1+Q}{2}J_v \\ \beta \end{bmatrix}_{\acute{\mathbf{r}}} = \begin{bmatrix} -\hat{\mathbf{v}} \\ \hat{\mathbf{u}} \\ \hat{\mathbf{n}} \\ -\hat{\mathbf{v}} \\ \hat{\mathbf{u}} \\ \hat{\mathbf{n}} \end{bmatrix}_{\acute{\mathbf{r}}} \cdot \sum_{i=1}^{N} \begin{bmatrix} \mathbf{a} & \mathbf{b} & \mathbf{e} & \mathbf{c} & \mathbf{d} & \mathbf{0}] \\ \mathbf{a} & \mathbf{b} & \mathbf{e} & \mathbf{c} & \mathbf{d} & \mathbf{0}] \\ \mathbf{a} & \mathbf{b} & \mathbf{e} & \mathbf{c} & \mathbf{d} & \mathbf{0}] \\ \mathbf{g} & \mathbf{h} & \mathbf{0} & \mathbf{a}_Q & \mathbf{b}_Q & \mathbf{f}] \\ \mathbf{g} & \mathbf{h} & \mathbf{0} & \mathbf{a}_Q & \mathbf{b}_Q & \mathbf{f}] \\ \mathbf{g} & \mathbf{h} & \mathbf{0} & \mathbf{a}_Q & \mathbf{b}_Q & \mathbf{f} \end{bmatrix} \begin{bmatrix} M_u] \\ M_v] \\ \alpha] \\ J_u] \\ J_v] \\ \beta \end{bmatrix}_{\mathbf{r}^i} + \begin{bmatrix} -\hat{\mathbf{v}} \cdot \sqrt{\chi_1}\mathbf{E}_{\Gamma_0+\Gamma_1} \\ \hat{\mathbf{u}} \cdot \sqrt{\chi_1}\mathbf{E}_{\Gamma_0+\Gamma_1} \\ \hat{\mathbf{n}} \cdot \sqrt{\chi_1}\mathbf{E}_{\Gamma_0+\Gamma_1} \\ -\hat{\mathbf{v}} \cdot \frac{\mathrm{i}\omega}{\sqrt{-\xi_1}}\mathbf{B}_{\Gamma_0+\Gamma_1} \\ \hat{\mathbf{u}} \cdot \frac{\mathrm{i}\omega}{\sqrt{-\xi_1}}\mathbf{B}_{\Gamma_0+\Gamma_1} \\ \hat{\mathbf{n}} \cdot \frac{\mathrm{i}\omega}{\sqrt{-\xi_1}}\mathbf{B}_{\Gamma_0+\Gamma_1} \end{bmatrix}_{\acute{\mathbf{r}}}, \tag{26}$$

where $\acute{\mathbf{r}}$ is the centre point of a given observation triangle, and $\mathbf{r}^i$ is the point of the ith source triangle. The various elements in the 6×6 matrix are given by

$$\mathbf{a} = \iint_{\triangle_i} \hat{\mathbf{u}} \times (\nabla\varphi_1 - \nabla\varphi_0)\, \mathrm{d}s, \tag{27}$$

$$\mathbf{b} = \iint_{\triangle_i} \hat{\mathbf{v}} \times (\nabla\varphi_1 - \nabla\varphi_0)\, \mathrm{d}s, \tag{28}$$

$$\mathbf{a}_Q = \iint_{\triangle_i} \hat{\mathbf{u}} \times (\nabla\varphi_1 - Q\nabla\varphi_0)\, \mathrm{d}s, \tag{29}$$

$$\mathbf{b}_Q = \iint_{\triangle_i} \hat{\mathbf{v}} \times (\nabla\varphi_1 - Q\nabla\varphi_0)\, \mathrm{d}s, \tag{30}$$

$$\mathbf{c} = \iint_{\triangle_i} k_1\,(\varphi_1 - Q\varphi_0)\,\hat{\mathbf{u}}\, \mathrm{d}s, \tag{31}$$

$$\mathbf{d} = \iint_{\triangle_i} k_1\,(\varphi_1 - Q\varphi_0)\,\hat{\mathbf{v}}\, \mathrm{d}s, \tag{32}$$

$$\mathbf{e} = \iint_{\triangle_i} (D\nabla\varphi_1 - \nabla\varphi_0)\, \mathrm{d}s, \tag{33}$$

$$\mathbf{f} = \iint_{\triangle_i} (\nabla\varphi_1 - \nabla\varphi_0)\, \mathrm{d}s, \tag{34}$$

$$\mathbf{g} = \iint_{\triangle_i} k_1 \left(\varphi_1 - Q D\varphi_0\right) \hat{\mathbf{u}} \, \mathrm{d}s, \tag{35}$$

$$\mathbf{h} = \iint_{\triangle_i} k_1 \left(\varphi_1 - Q D\varphi_0\right) \hat{\mathbf{v}} \, \mathrm{d}s. \tag{36}$$

When the observation point is located inside the source triangle $\triangle_i$, the surface integrals in the above eqs (27)–(36) become singular. A singularity extraction technique (Ylä-Oijala & Taskinen 2003; Ren *et al.* 2010), which analytically evaluates the singular parts is therefore adopted to accurately compute the values of those integrals having singular integrands.

The above procedure is followed for all triangles, to finally yield a system of linear equations of dimensions $6N \times 6N$

$$\mathbf{AX} = \mathbf{Y}, \tag{37}$$

where $\mathbf{X} = \{\mathbf{X}_i, i = 0, 1, \ldots, N-1\}$, $\mathbf{X}_i = \{M_u, M_v, \alpha, J_u, J_v, \beta\}_i$ are the unknown surface currents and charges over the ith triangle. It should be noted that the final system matrix $\mathbf{A}$ of eq. (37) is diagonally dominant, which indicates its favourable behaviour and low condition number (see Section A4). For the specific case of a homogeneous full space model, the system matrix becomes the identity matrix, with a condition number of one. The right-hand side vector $\mathbf{Y}$ depends on the polarization and the azimuthal and inclination angles of the incident wave.

For a single observation point, the integral eqs (27)–(36) need to be evaluated over all N triangles which constitute Γ, due to the interactions between the Green's functions. Therefore, the algorithm has a $O(m^2)$ time complexity and a memory cost of $O(m^2)$ to compute and store all terms in the final system of linear eq. (37), respectively, where $m = 6N$. To solve this full system of linear equations by direct solvers, a time cost of about $O(m^3)$ is required. For small-scale problems in which the number of unknowns is less than a few thousand, we apply the open source MUMPS library (Amestoy *et al.* 2002; Operto *et al.* 2007; Streich 2009) to directly solve the linear system (37). We refer to this as the standard BEM in the remainder of the paper.

ADAPTIVE MULTILEVEL FAST MULTIPOLE BEM METHOD

The expensive computational cost of $O(m^2)$ complexity for explicitly assembling and storing the system matrix makes the standard BEM incapable of handing large-scale problems, in which the number of unknowns is typically tens or hundreds of thousands. To overcome this limitation of the standard BEM algorithm, an adaptive multilevel fast multipole BEM (AMFM-BEM; Hackbusch & Nowak 1989; Buchau *et al.* 2000) was introduced and further developed by us. Due to its complicated theoretical analysis and non-trivial implementation, only a few applications of the AMFM approach have been published in geophysics, such as the scalar gravity field problem (May & Knepley 2011), the direct current resistivity problem (Blome *et al.* 2009) and the seismic wave problem (Fujiwara 2000; Çakır 2006, 2009). To the best of our knowledge, this study is the first attempt to use the AMFM concept to study 3-D geo-electromagnetic problems. Additionally, in terms of the concept of panel clustering (Hackbusch & Nowak 1989), two optimal sub-algorithms are introduced to simplify the implementation of the original procedure of the AMFM algorithm (Liu 2009) and to optimize its performance (see Section A1 and A2 for details).

Instead of explicitly assembling the system matrix $\mathbf{A}$, the AMFM-BEM method which incorporates the generalized minimal residual solver [GMRES, embedded in the open source PETSc library (Balay *et al.* 2010)] seeks to rapidly compute the product of the system matrix with an initial vector of unknowns. Under this framework, the system matrix $\mathbf{A}$ can be divided into a banded matrix $\mathbf{A}_{\text{near}}$ and an off-diagonal matrix $\mathbf{A}_{\text{far}}$. Here, the banded matrix $\mathbf{A}_{\text{near}}$ with several non-zeros around the main diagonal stands for the near field integrals over nearby triangles and is a sparse matrix. The off-diagonal matrix $\mathbf{A}_{\text{far}}$ stands for the far-field integrals and is partially dense. Using this decomposition, the multiplication of the system matrix with the initial vector of unknowns can be represented as

$$\mathbf{AX} = \mathbf{A}_{\text{near}}\mathbf{X} + \mathbf{A}_{\text{far}}\mathbf{X}. \tag{38}$$

Due to the sparse nature of the banded matrix $\mathbf{A}_{\text{near}}$, the computation only requires a linear $O(m)$ time and memory complexity to perform the first multiplication $\mathbf{A}_{\text{near}}\mathbf{X}$. Exploiting the features of the AMFM aglorithm, the time complexity of performing the multiplication $\mathbf{A}_{\text{far}}\mathbf{X}$ is reduced to $O(m \log m)$ and the memory cost reduced to $O(m)$, at each iteration of the GMRES solver. Assuming the number of iterations used by the GMRES solver is n_{it}, the total time complexity of the AMFM-BEM algorithm is only about $O(n_{it} m \log m)$.

Multipole moments

The core integrals in the multiplication $\mathbf{A}_{\text{far}}\mathbf{X}$ in eq. (38) for an arbitrary given observation point $\acute{\mathbf{r}}$ are

$$\mathbf{I}_{(\acute{\mathbf{r}})} = \iint_{\mathbf{r}\in\Gamma_{\text{far}}} \left[\mathbf{M} \times \left(\nabla\varphi_1 - \nabla\varphi_0\right) + k_1 \mathbf{J} \left(\varphi_1 - Q\varphi_0\right) + \alpha \left(D\nabla\varphi_1 - \nabla\varphi_0\right)\right] \mathrm{d}s, \tag{39}$$

$$\mathbf{II}_{(\acute{\mathbf{r}})} = \iint_{\mathbf{r}\in\Gamma_{\text{far}}} \left[\mathbf{J} \times \left(\nabla\varphi_1 - Q\nabla\varphi_0\right) + k_1 \mathbf{M} \left(\varphi_1 - Q D\varphi_0\right) + \beta \left(\nabla\varphi_1 - \nabla\varphi_0\right)\right] \mathrm{d}s, \tag{40}$$

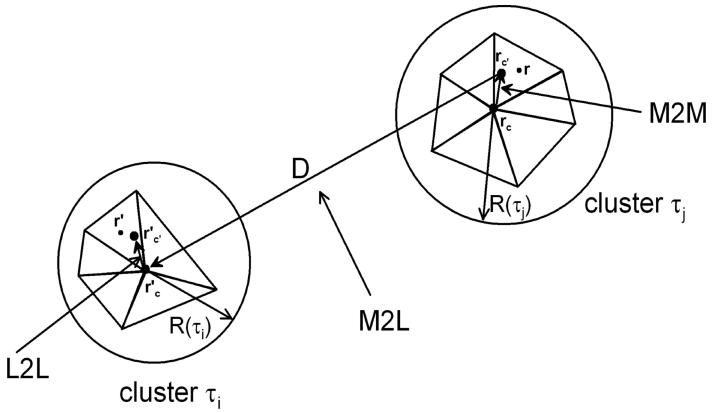

Figure 2. Direct connections between observation points $\acute{\mathbf{r}}$ and source points $\mathbf{r}$ are represented by moments-to-moments transformations (**M2M**), moments-to-local transformations (**M2L**) and local-to-local transformations (**L2L**). Observation points of observation triangles are grouped into a cluster τ_i having radius $R(\tau_i)$ and source points of source triangles are grouped into a cluster τ_j having radius $R(\tau_j)$. The quantity $\mathbf{r}_c$ is the multipole expansion centre of the cube which contains the source points; $\mathbf{r}_{\acute{c}}$ is the expansion centre of the parent cube with the child cube containing the source points. Quantity $\acute{\mathbf{r}}_c$ is the local expansion centre of a parent cube which contains the observation point; $\acute{\mathbf{r}}_{\acute{c}}$ is the local centre of a child cube with its parent cube containing the observation point. If the distance D between clusters τ_i and τ_j satisfies the admissible condition, $D(\tau_i, \tau_j) \geq \gamma \max[R(\tau_i), R(\tau_j)]$, then clusters τ_i and τ_j are in a far-field configuration, otherwise in a near-field configuration, where $\gamma > 0$ is the admissible factor. The optimal admissible factor γ is about 2.0 (shown in Fig. 3) for our study.

where $\mathbf{r} \in \Gamma_{\text{far}}$ denotes the integral domain far away from the observation point $\acute{\mathbf{r}}$.

According to Gegenbauer's addition theorem (Abramowitz & Stegun 1964), if the source point $\mathbf{r} \in \Gamma_{\text{far}}$ and the observation point $\acute{\mathbf{r}}$ are sufficiently far away from each other, the interaction between $\mathbf{r}$ and $\acute{\mathbf{r}}$ via the Green's functions can be separated in terms of an expansion point $\mathbf{r}_c$ around the source point $\mathbf{r}$ (shown in Fig. 2). Hence, for $|\mathbf{r} - \mathbf{r}_c| < |\acute{\mathbf{r}} - \mathbf{r}_c|$

$$\varphi(k, \acute{\mathbf{r}}, \mathbf{r}) = \frac{\mathrm{e}^{\mathrm{i}k|\acute{\mathbf{r}}-\mathbf{r}|}}{4\pi|\acute{\mathbf{r}}-\mathbf{r}|} = \frac{\mathrm{i}k}{4\pi}\sum_{n=0}^{\infty}(2n+1)\sum_{m=-n}^{n} S_n^{-m}(k, \acute{\mathbf{r}}-\mathbf{r}_c)\, R_n^m(k, \mathbf{r}-\mathbf{r}_c), \tag{41}$$

where $\varphi(k, \acute{\mathbf{r}}, \mathbf{r})$ is the Green's function of the 3-D Helmholtz equation in the full space, and k is the complex wavenumber. For the wavenumber k_0 in Ω_0, we write in short $\varphi(k_0) = \varphi_0$. Similarly, $\varphi(k_1)$ is designated as φ_1. $S_n^m(k, \vec{\mathbf{x}})$ are the solid harmonics, which are singular as $\vec{\mathbf{x}} \to \mathbf{0}$, and $R_n^m(k, \vec{\mathbf{x}})$ are the regular solid harmonics as $\vec{\mathbf{x}} \to \mathbf{0}$. The solid harmonics are defined in terms of the spherical harmonics $Y_n^m(\theta, \phi)$, that is,

$$S_n^m(k, \vec{\mathbf{x}}) = h_n^{(1)}(kr)\, Y_n^m(\theta, \phi) \tag{42}$$

$$R_n^m(k, \vec{\mathbf{x}}) = j_n(kr)\, Y_n^m(\theta, \phi). \tag{43}$$

Here $h_n^{(1)}$ and j_n are the spherical Bessel functions of the third and first kind, respectively, (r, θ, ϕ) represent the spherical coordinates of an arbitrary vector $\vec{\mathbf{x}}$, $0 \leq \theta \leq \pi$, $0 \leq r < \infty$, $0 \leq \phi < 2\pi$, and the spherical harmonics $Y_n^m(\theta, \phi)$ are defined by

$$Y_n^m(\theta, \phi) = (-1)^m \sqrt{\frac{(n-|m|)!}{(n+|m|)!}} P_n^{|m|}(\cos\theta)\, e^{im\phi}, \quad n \geq 0, \quad -n \geq m \geq n, \tag{43}$$

with P_n^m the associated Legendre functions and $P_n^0 = P_n$ the Legendre polynomials. Substituting the expansion expression (41) of $\varphi(k, \acute{\mathbf{r}}, \mathbf{r})$ into eqs (39) and (40), we have

$$\begin{pmatrix} \mathbf{I}_{\text{far}} \\ \mathbf{II}_{\text{far}} \end{pmatrix}_{\acute{\mathbf{r}}} = \sum_{n=0}^{\infty}\sum_{m=-n}^{n} \begin{pmatrix} \mathbf{S}_{\text{I}}^{nm}(\acute{\mathbf{r}}-\mathbf{r}_c) \cdot [\mathbf{M}_{\text{I}}^{nm}(\mathbf{r}_c)]^T \\ \mathbf{S}_{\text{II}}^{nm}(\acute{\mathbf{r}}-\mathbf{r}_c) \cdot [\mathbf{M}_{\text{II}}^{nm}(\mathbf{r}_c)]^T \end{pmatrix}, \quad |\acute{\mathbf{r}}-\mathbf{r}_c| > |\mathbf{r}-\mathbf{r}_c|, \tag{44}$$

where $\cdot$ is the dot operator, T is a transposition operator, $\mathbf{S}_{\text{I}}$ and $\mathbf{S}_{\text{II}}$ are the moment basis functions given by

$$\begin{aligned} \mathbf{S}_{\text{I}}^{nm}(\vec{\mathbf{x}}) = \frac{\mathrm{i}(2n+1)}{4\pi}\big[& S_n^{-m}(k_1, \vec{\mathbf{x}})k_1, -S_n^{-m}(k_0, \vec{\mathbf{x}})k_0, S_n^{-m}(k_1, \vec{\mathbf{x}})k_1^2, \\ & -S_n^{-m}(k_0, \vec{\mathbf{x}})k_0k_1\, Q, S_n^{-m}(k_1, \vec{\mathbf{x}})k_1\, D, -S_n^{-m}(k_0, \vec{\mathbf{x}})k_0\big], \end{aligned} \tag{45}$$

$$\begin{aligned} \mathbf{S}_{\text{II}}^{nm}(\vec{\mathbf{x}}) = \frac{\mathrm{i}(2n+1)}{4\pi}\big[& S_n^{-m}(k_1, \vec{\mathbf{x}})k_1, -S_n^{-m}(k_0, \vec{\mathbf{x}})Qk_0, S_n^{-m}(k_1, \vec{\mathbf{x}})k_1^2, \\ & -S_n^{-m}(k_0, \vec{\mathbf{x}})k_0k_1\, QD, S_n^{-m}(k_1, \vec{\mathbf{x}})k_1, -S_n^{-m}(k_0, \vec{\mathbf{x}})k_0\big], \end{aligned} \tag{46}$$

and $\mathbf{M}_{\mathrm{I}}$ and $\mathbf{M}_{\mathrm{II}}$ are the multipole moments (MM) which are independent of the observation point. The explicit forms of the multipole moments centred at $\mathbf{r}_{\mathrm{c}}$ are

$$\mathbf{M}_{\mathrm{I}}^{nm}(\mathbf{r}_{\mathrm{c}}) = \sum_{i=0}^{N_{\mathrm{far}}-1} \big[\mathbf{M}_i \times \mathbf{M}_i^{\nabla nm}(k_1, \mathbf{r}_{\mathrm{c}}), \mathbf{M}_i \times \mathbf{M}_i^{\nabla nm}(k_0, \mathbf{r}_{\mathrm{c}}), \mathbf{J}_i M_i^{nm}(k_1, \mathbf{r}_{\mathrm{c}}), \mathbf{J}_i M_i^{nm}(k_0, \mathbf{r}_{\mathrm{c}}), \ \alpha_i \mathbf{M}_i^{\nabla nm}(k_1, \mathbf{r}_{\mathrm{c}}), \ \alpha_i \mathbf{M}_i^{\nabla nm}(k_0, \mathbf{r}_{\mathrm{c}})\big],$$

$$\mathbf{M}_{\mathrm{II}}^{nm}(\mathbf{r}_{\mathrm{c}}) = \sum_{i=0}^{N_{\mathrm{far}}-1} \big[\mathbf{J}_i \times \mathbf{M}_i^{\nabla nm}(k_1, \mathbf{r}_{\mathrm{c}}), \mathbf{J}_i \times \mathbf{M}_i^{\nabla nm}(k_0, \mathbf{r}_{\mathrm{c}}), \mathbf{M}_i M_i^{nm}(k_1, \mathbf{r}_{\mathrm{c}}), \mathbf{M}_i M_i^{nm}(k_0, \mathbf{r}_{\mathrm{c}}), \ \beta_i \mathbf{M}_i^{\nabla nm}(k_1, \mathbf{r}_{\mathrm{c}}), \ \beta_i \mathbf{M}_i^{\nabla nm}(k_0, \mathbf{r}_{\mathrm{c}})\big],$$

where N_{far} is the number of triangles in Γ_{far}, $\mathbf{M}_i$, $\mathbf{J}_i$, α_i and β_i are constant distributions of surface currents and charges over each triangle, $\triangle_i \in \Gamma_{\mathrm{far}}$, and the multipole moments over a single triangle are (see Appendix B for details)

$$\mathbf{M}_i^{\nabla nm}(k, \mathbf{r}_{\mathrm{c}}) = \iint_{\mathbf{r}\in\triangle_i} \nabla R_n^m(k, \mathbf{r} - \mathbf{r}_{\mathrm{c}})\, \mathrm{d}s, \tag{47}$$

$$M_i^{nm}(k, \mathbf{r}_{\mathrm{c}}) = \iint_{\mathbf{r}\in\triangle_i} R_n^m(k, \mathbf{r} - \mathbf{r}_{\mathrm{c}})\, \mathrm{d}s. \tag{48}$$

M2M, M2L and L2L transformations

As observed from eq. (44), the fundamental reason for the reduction in the number of operations in the fast multipole accelerated BEM approach is that once the multipole moments are computed at the expansion centre $\mathbf{r}_{\mathrm{c}}$, for a moving observation point $\acute{\mathbf{r}}$, the evaluations of these new far-field integrals require simple algebraic operations. The given surface Γ (such as the air–Earth interface) which is composed of m small disjoint triangles is divided into k regions (each region should act as both observation and source region). For the nth ($n = 1, ..., k$) observation region (we assume that both it and its abutting regions contain m_n triangles), the direct computation of the singular or nearly singular integrals in $\mathbf{A}_{\mathrm{near}}$ requires $O(m_n^2)$ operations. The computation of the multipole moments ($\mathbf{M}_{\mathrm{I}}$ and $\mathbf{M}_{\mathrm{II}}$ in eq. 44) over the far-field regions requires $O[(m - m_n)p^2]$ operations, where p is the truncation number of the expansion series used in eq. (44). The evaluation of the moment basic functions ($\mathbf{S}_{\mathrm{I}}$ and $\mathbf{S}_{\mathrm{II}}$ in eq. 44) needs $O(m_n p^2)$ operations. Therefore, the complexity function $F(k)$ involving only the procedure for multipole moment expansions (using eq. 44) is $F(k) = \sum_{n=1}^{k}[m_n^2 + (m - m_n)p^2 + m_n p^2]$. Assuming that the given surface Γ is uniformly divided which means $m_n = \frac{m}{k}$, then the minimum value of $F(k)$ is given by

$$F(k) = \frac{m^2}{k} + kp^2 m \tag{49}$$

$$F(k)_{\min} = 2m^{\frac{3}{2}} p = O(m^{3/2}), \qquad k_{\min} = \frac{\sqrt{m}}{p}. \tag{50}$$

The above algorithm is also referred as the single level fast multipole method (Liu 2009). It offers an $O(m^{3/2})$ time complexity. To achieve an optimal $O(m \log m)$ time complexity at each iteration, the adaptive multilevel fast multipole method is adopted in which the three transformations (M2M, M2L and L2L) are needed, the basic theory for which is now outlined.

Moments to moments (M2M) transformation

If the multipole expansion centre $\mathbf{r}_{\mathrm{c}}$ is shifted to another expansion centre $\mathbf{r}_{\acute{\mathrm{c}}}$ of Γ_{far} (shown in Fig. 2), the far-field integrals over Γ_{far} with centre $\mathbf{r}_{\acute{\mathrm{c}}}$ can be presented in a similar form as eq. (44)

$$\begin{pmatrix} \mathbf{I}_{\mathrm{far}} \\ \mathbf{II}_{\mathrm{far}} \end{pmatrix}_{\acute{\mathbf{r}}} = \sum_{n=0}^{\infty}\sum_{m=-n}^{n} \begin{pmatrix} \mathbf{S}_{\mathrm{I}}^{nm}(\acute{\mathbf{r}} - \mathbf{r}_{\acute{\mathrm{c}}}) \cdot [\mathbf{M}_{\mathrm{I}}^{nm}(\mathbf{r}_{\acute{\mathrm{c}}})]^T \\ \mathbf{S}_{\mathrm{II}}^{nm}(\acute{\mathbf{r}} - \mathbf{r}_{\acute{\mathrm{c}}}) \cdot [\mathbf{M}_{\mathrm{II}}^{nm}(\mathbf{r}_{\acute{\mathrm{c}}})]^T \end{pmatrix}, \quad |\acute{\mathbf{r}} - \mathbf{r}_{\acute{\mathrm{c}}}| > |\mathbf{r} - \mathbf{r}_{\acute{\mathrm{c}}}|. \tag{51}$$

Here, the new multipole moments $\mathbf{M}_{\mathrm{I}}^{nm}(\mathbf{r}_{\acute{\mathrm{c}}})$ and $\mathbf{M}_{\mathrm{II}}^{nm}(\mathbf{r}_{\acute{\mathrm{c}}})$ can be computed by $\mathbf{M}_{\mathrm{I}}^{nm}(\mathbf{r}_{\mathrm{c}})$ and $\mathbf{M}_{\mathrm{II}}^{nm}(\mathbf{r}_{\mathrm{c}})$ as follows. According to the convolution form of the Helmholtz translation theorem (Epton & Dembart 1995), the regular solid harmonics in eq. (43) fulfill the requirement:

$$\begin{aligned} R_n^m(k, \mathbf{r} - \mathbf{r}_{\acute{\mathrm{c}}}) &= R_n^m(k, \mathbf{r} - \mathbf{r}_{\mathrm{c}} + \mathbf{r}_{\mathrm{c}} - \mathbf{r}_{\acute{\mathrm{c}}}) \\ &= \sum_{\acute{n}=0}^{\infty}\sum_{\acute{m}=-\acute{n}}^{\acute{n}}\sum_{s=0}^{n+\acute{n}-2a} \frac{(2s+1)(2\acute{n}+1)}{4\pi}(-1)^a E \begin{pmatrix} m & \acute{m} & -j \\ n & \acute{n} & s \end{pmatrix} R_{\acute{n}}^{-\acute{m}}(k, \mathbf{r}_{\acute{\mathrm{c}}} - \mathbf{r}_{\mathrm{c}})\, R_s^j(k, \mathbf{r} - \mathbf{r}_{\mathrm{c}}) \\ &= \sum_{\acute{n}=0}^{\infty}\sum_{\acute{m}=-\acute{n}}^{\acute{n}}\sum_{s=0}^{n+\acute{n}-2a} (R|R)_{nm}^{\acute{n}\acute{m}s} R_{\acute{n}}^{-\acute{m}}(k, \mathbf{r}_{\acute{\mathrm{c}}} - \mathbf{r}_{\mathrm{c}})\, R_s^j(k, \mathbf{r} - \mathbf{r}_{\mathrm{c}}), \\ &\quad (j = m + \acute{m}, \quad a \geq 0), \end{aligned}$$

where $\acute{n}, \acute{m}, s, n, m$ and a are integers, and integer a is chosen from $a = \frac{1}{2}(n + \acute{n} - s) \geq 0$, $(R|R)_{nm}^{\acute{n}\acute{m}s}$ are the abbreviations for the first three factors in the second line of the above equation, and $E\left(\begin{smallmatrix} * & * & * \\ * & * & * \end{smallmatrix}\right)$ are the Wigner 3-j symbols (Abramowitz & Stegun 1964), which are evaluated using the open source GNU scientific library (Galassi *et al.* 2009). Using the above identity and considering both eqs (51) and (44), we have the following M2M transformation to evaluate the new multipole moments centred at $\mathbf{r}_{\acute{c}}$ by the multipole moments centred at $\mathbf{r}_{c}$

$$\begin{bmatrix} \mathbf{M}_{\mathrm{I}}^{nm}(\mathbf{r}_{\acute{c}}) \\ \mathbf{M}_{\mathrm{II}}^{nm}(\mathbf{r}_{\acute{c}}) \end{bmatrix} = \sum_{\acute{n}=0}^{\infty} \sum_{\acute{m}=-\acute{n}}^{\acute{n}} \sum_{s=0}^{n+\acute{n}-2a} (\mathbf{M2M})_{nm}^{\acute{n}\acute{m}s}(\mathbf{r}_{\acute{c}} - \mathbf{r}_{c}) \cdot \begin{bmatrix} \mathbf{M}_{\mathrm{I}}^{sj}(\mathbf{r}_{c}) \\ \mathbf{M}_{\mathrm{II}}^{sj}(\mathbf{r}_{c}) \end{bmatrix}. \tag{52}$$

Moments to local (M2L) transformation

We assume that $\acute{\mathbf{r}}_{c}$ is the local expansion centre of the observation point (shown in Fig. 2), $\mathbf{r}$ is far away from the observation point so that $|\acute{\mathbf{r}} - \acute{\mathbf{r}}_{c}| < |\mathbf{r} - \acute{\mathbf{r}}_{c}|$, the Green's functions can be rewritten as

$$\varphi(k, \acute{\mathbf{r}}, \mathbf{r}) = \frac{e^{\mathrm{i}k|\acute{\mathbf{r}}-\mathbf{r}|}}{4\pi|\acute{\mathbf{r}} - \mathbf{r}|} = \frac{\mathrm{i}k}{4\pi} \sum_{n=0}^{\infty}(2n+1) \sum_{m=-n}^{n} R_{n}^{-m}(k, \acute{\mathbf{r}} - \acute{\mathbf{r}}_{c})\, S_{n}^{m}(k, \mathbf{r} - \acute{\mathbf{r}}_{c}). \tag{53}$$

Substituting the above local expansion into eqs (39) and (40), for Γ_{far}, with respect to $\acute{\mathbf{r}}$, this yields

$$\begin{pmatrix} \mathbf{I}_{\mathrm{far}} \\ \mathbf{II}_{\mathrm{far}} \end{pmatrix}_{\acute{\mathbf{r}}} = \sum_{n=0}^{\infty} \sum_{m=-n}^{n} \begin{pmatrix} \mathbf{R}_{\mathrm{I}}^{nm}(\acute{\mathbf{r}} - \acute{\mathbf{r}}_{c}) \centerdot [\mathbf{L}_{\mathrm{I}}^{nm}(\acute{\mathbf{r}}_{c})]^{T} \\ \mathbf{R}_{\mathrm{II}}^{nm}(\acute{\mathbf{r}} - \acute{\mathbf{r}}_{c}) \centerdot [\mathbf{L}_{\mathrm{II}}^{nm}(\acute{\mathbf{r}}_{c})]^{T} \end{pmatrix}, \quad |\acute{\mathbf{r}} - \acute{\mathbf{r}}_{c}| < |\mathbf{r} - \acute{\mathbf{r}}_{c}|. \tag{54}$$

Here $\mathbf{R}_{\mathrm{I}}^{nm}(\vec{\mathbf{x}})$ and $\mathbf{R}_{\mathrm{II}}^{nm}(\vec{\mathbf{x}})$ are the local expansion basis functions, for $\vec{\mathbf{x}} = \acute{\mathbf{r}} - \acute{\mathbf{r}}_{c}$ which are similar to eqs (45) and (46), that is,

$$\begin{aligned} \mathbf{R}_{\mathrm{I}}^{nm}(\vec{\mathbf{x}}) = \frac{i(2n+1)}{4\pi} \big[& R_{n}^{-m}(k_1, \vec{\mathbf{x}})k_1, -R_{n}^{-m}(k_0, \vec{\mathbf{x}})k_0, R_{n}^{-m}(k_1, \vec{\mathbf{x}})k_1^2, \\ & - R_{n}^{-m}(k_0, \vec{\mathbf{x}})k_0 k_1 Q, R_{n}^{-m}(k_1, \vec{\mathbf{x}})k_1 D, -R_{n}^{-m}(k_0, \vec{\mathbf{x}})k_0 \big], \end{aligned} \tag{55}$$

$$\begin{aligned} \mathbf{R}_{\mathrm{II}}^{nm}(\vec{\mathbf{x}}) = \frac{i(2n+1)}{4\pi} \big[& R_{n}^{-m}(k_1, \vec{\mathbf{x}})k_1, -R_{n}^{-m}(k_0, \vec{\mathbf{x}})Qk_0, R_{n}^{-m}(k_1, \vec{\mathbf{x}})k_1^2, \\ & -R_{n}^{-m}(k_0, \vec{\mathbf{x}})k_0 k_1 QD, R_{n}^{-m}(k_1, \vec{\mathbf{x}})k_1, -R_{n}^{-m}(k_0, \vec{\mathbf{x}})k_0 \big]. \end{aligned} \tag{56}$$

Using the addition theorem (Epton & Dembart 1995; Gumerov & Duraiswami 2004b) for the singular solid harmonics in eq. (42), we obtain

$$\begin{aligned} S_{n}^{m}(k, \mathbf{r} - \acute{\mathbf{r}}_{c}) &= S_{n}^{m}(k, \mathbf{r} - \mathbf{r}_{\acute{c}} + \mathbf{r}_{\acute{c}} - \acute{\mathbf{r}}_{c}) \\ &= \sum_{\acute{n}=0}^{\infty} \sum_{\acute{m}=-\acute{n}}^{\acute{n}} \sum_{s=0}^{n+\acute{n}-2a} (S|R)_{nm}^{\acute{n}\acute{m}s} (-1)^{s+\acute{n}} S_{s}^{j}(k, \acute{\mathbf{r}}_{c} - \mathbf{r}_{\acute{c}})\, R_{\acute{n}}^{-\acute{m}}(k, \mathbf{r} - \mathbf{r}_{\acute{c}}), \end{aligned} \tag{57}$$

where $(S|R)_{nm}^{\acute{n}\acute{m}s} = (R|R)_{nm}^{\acute{n}\acute{m}s}$. Substituting the above result into eq. (54), the local expansion coefficients centred at the local point $\acute{\mathbf{r}}_{c}$ can be represented by the new multipole moments centred at the multipole point $\mathbf{r}_{\acute{c}}$ by the following M2L transformation

$$\begin{bmatrix} \mathbf{L}_{\mathrm{I}}^{nm}(\acute{\mathbf{r}}_{c}) \\ \mathbf{L}_{\mathrm{I}}^{nm}(\acute{\mathbf{r}}_{c}) \end{bmatrix} = \sum_{\acute{n}=0}^{\infty} \sum_{\acute{m}=-\acute{n}}^{\acute{n}} \sum_{s=0}^{n+\acute{n}-2a} (\mathbf{M2L})_{nm}^{\acute{n}\acute{m}s}(\acute{\mathbf{r}}_{c} - \mathbf{r}_{\acute{c}}) \cdot \begin{bmatrix} \mathbf{M}_{\mathrm{I}}^{\acute{n},-\acute{m}}(\mathbf{r}_{\acute{c}}) \\ \mathbf{M}_{\mathrm{I}}^{\acute{n},-\acute{m}}(\mathbf{r}_{\acute{c}}) \end{bmatrix}. \tag{58}$$

Local to local (L2L) transformation

If the local expansion point $\acute{\mathbf{r}}_{c}$ is shifted to another local expansion point $\acute{\mathbf{r}}_{\acute{c}}$ (shown in Fig. 2), the far-field contributions centred at the new local expansion point $\acute{\mathbf{r}}_{\acute{c}}$ can be rewritten as

$$\begin{pmatrix} \mathbf{I}_{\mathrm{far}} \\ \mathbf{II}_{\mathrm{far}} \end{pmatrix}_{\acute{\mathbf{r}}} = \sum_{n=0}^{\infty} \sum_{m=-n}^{n} \begin{pmatrix} \mathbf{R}_{\mathrm{I}}^{nm}(\acute{\mathbf{r}} - \acute{\mathbf{r}}_{\acute{c}}) \centerdot [\mathbf{L}_{\mathrm{I}}^{nm}(\acute{\mathbf{r}}_{\acute{c}})]^{T} \\ \mathbf{R}_{\mathrm{II}}^{nm}(\acute{\mathbf{r}} - \acute{\mathbf{r}}_{\acute{c}}) \centerdot [\mathbf{L}_{\mathrm{II}}^{nm}(\acute{\mathbf{r}}_{\acute{c}})]^{T} \end{pmatrix}, \quad |\acute{\mathbf{r}} - \acute{\mathbf{r}}_{\acute{c}}| < |\mathbf{r} - \acute{\mathbf{r}}_{\acute{c}}|. \tag{59}$$

Due to the availability of the local expansion coefficients $\mathbf{L}_{\mathrm{I}}^{nm}(\acute{\mathbf{r}}_{c})$ and $\mathbf{L}_{\mathrm{II}}^{nm}(\acute{\mathbf{r}}_{c})$ at the old local expansion point, reusing the old local expansion coefficients to compute the new local expansion coefficients (centred at $\acute{\mathbf{r}}_{\acute{c}}$) is faster than directly evaluating these new local expansion coefficients (Liu 2009). We also have (Epton & Dembart 1995; Gumerov & Duraiswami 2004b), $S_{n}^{m}(k, \mathbf{r} - \acute{\mathbf{r}}_{\acute{c}}) = S_{n}^{m}(k, \mathbf{r} - \acute{\mathbf{r}}_{c} + \acute{\mathbf{r}}_{c} - \acute{\mathbf{r}}_{\acute{c}})$, $|\mathbf{r} - \acute{\mathbf{r}}_{c}| > |\acute{\mathbf{r}}_{c} - \acute{\mathbf{r}}_{\acute{c}}|$, which yields

$$S_{n}^{m}(k, \mathbf{r} - \acute{\mathbf{r}}_{\acute{c}}) = \sum_{\acute{n}=0}^{\infty} \sum_{\acute{m}=-\acute{n}}^{\acute{n}} \sum_{s=0}^{n+\acute{n}-2a} (S|S)_{nm}^{\acute{n}\acute{m}s} R_{\acute{n}}^{-\acute{m}}(k, \acute{\mathbf{r}}_{\acute{c}} - \acute{\mathbf{r}}_{c})\, S_{s}^{j}(k, \mathbf{r} - \acute{\mathbf{r}}_{c}), \tag{60}$$

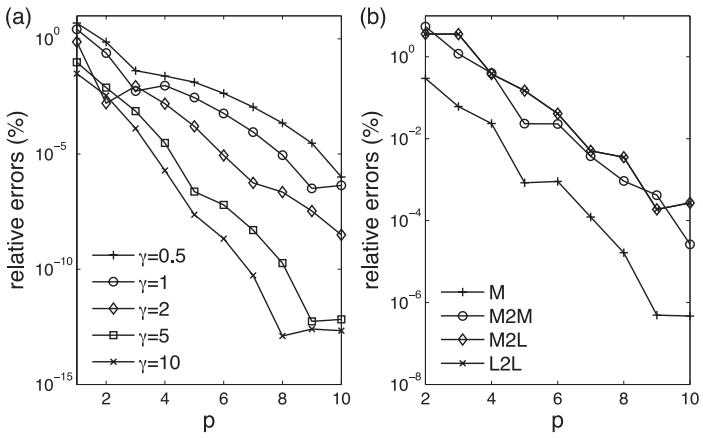

Figure 3. (a) Relative errors of multipole moments (**MM**) expansions of Green's functions over clusters τ_i and τ_j (in Fig. 2) versus the number of expansion terms (p), for different distance parameters γ. The clusters τ_i and τ_j are smaller than 0.1 skin depth in diameter. Numerical results suggest that with $\gamma = 2.0$, the number of expansion terms $p \geq 6$ would yield highly accurate results. (b) Relative errors of multipole moments (**MM**) expansions (eq. 44), **M2M** (eqs 51 and 52, **M2L** eqs 54 and 58 and **L2L** eqs 59 and 61) transformations versus the number of expansion terms (p), where $\gamma = 2.0$. The plot suggests that to guarantee a relative error of less than 0.01 per cent for all transformations, the number of expansion terms might be $p \geq 6$. In this numerical experiment, relative errors are measured against the semi-analytical evaluations of the surface integrals $\mathbf{I}_{\text{far}}$ and $\mathbf{II}_{\text{far}}$ in eqs (39) and (40) over two distant triangles with $\gamma = 2.0$. Numerical solutions for the **M2M** transformation are computed by the evaluated multipole moments; those for the **M2L** transformation are computed by the **M2M** transformation and so on. Therefore, the relative errors increase when the transformations are successively performed. As for the **L2L** transformation, due to the regular transformation core **L2L** in eqs (60) and (61), the **L2L** transformation shows an accuracy similar to that of the **M2L** transformation.

where $(S|S)_{nm}^{\acute{n}\acute{m}s} = (R|R)_{nm}^{\acute{n}\acute{m}s}$. Using eq. (60) and considering the implicit expressions for $\mathbf{L}_{\text{I}}^{nm}$ and $\mathbf{L}_{\text{II}}^{nm}$ in eq. (54), the new local expansion coefficients (centred at $\acute{\mathbf{r}}_{\acute{c}}$) can be represented by the old local expansion coefficients (centred at $\acute{\mathbf{r}}_{\text{c}}$) using the following L2L transformations

$$\begin{bmatrix} \mathbf{L}_{\text{I}}^{nm}(\acute{\mathbf{r}}_{\acute{c}}) \\ \mathbf{L}_{\text{II}}^{nm}(\acute{\mathbf{r}}_{\acute{c}}) \end{bmatrix} = \sum_{\acute{n}=0}^{\infty} \sum_{\acute{m}=-\acute{n}}^{\acute{n}} \sum_{s=0}^{n+\acute{n}-2a} (\mathbf{L2L})_{nm}^{\acute{n}\acute{m}s}(\acute{\mathbf{r}}_{\acute{c}} - \acute{\mathbf{r}}_{\text{c}}) \begin{bmatrix} \mathbf{L}_{\text{I}}^{sj}(\acute{\mathbf{r}}_{\text{c}}) \\ \mathbf{L}_{\text{II}}^{sj}(\acute{\mathbf{r}}_{\text{c}}) \end{bmatrix}. \tag{61}$$

Due to the summation over five integers ($n \geq 0, n \geq m \geq -n, \acute{n} \geq 0, \acute{n} \geq \acute{m} \geq -\acute{n}, s = n + \acute{n} - 2a, a \geq 0$), all three transformations need $O(p^5)$ operators, where $p \geq n \geq 0$ in the M2M and M2L and L2L transformation. For the case of large p, these transformations require a lot of computation time which decreases the efficiency of the fast multipole approach. Several algorithms were proposed to decrease the time complexity of these transformations, such as the diagonal form approach (Rokhlin 1992). However, the diagonal form becomes inaccurate at low frequency (Liu 2009). To avoid low-frequency problems, for local expansion coefficients $\mathbf{L}_{\text{I}}^{nm}(\acute{\mathbf{r}}_{\text{c}})$ and $\mathbf{L}_{\text{II}}^{nm}(\acute{\mathbf{r}}_{\text{c}})$ we adhere to using the original $O(p^5)$ algorithm. Typically, at MT and RMT frequencies, $p \leq 10$, based on numerical experiments (see Fig. 3). To improve the efficiency of these transformations, it might be valuable to investigate the potentials of an $O(p^3)$ algorithm which was proposed by Gumerov & Duraiswami (2004b) in the future.

Transformations on a cluster tree

To efficiently perform these three transformations, a hierarchy cluster tree Υ needs to be set up by using the cluster tree construction algorithm presented in Section A1. On this tree, the disjoint triangles of the given air–Earth interface Γ are adaptively distributed into cluster cells. Selecting an arbitrary leaf cluster cell τ on Υ, using the generalized cluster relationship identification algorithm presented in Section A2, its far field clusters P_{far}, near field clusters P_{near} and interaction-field clusters P_{inter} can be found. After the upward and downward pass procedures (which are presented in Section A3), the far-field integral term $\mathbf{A}_{\text{far}}\mathbf{X}$ over P_{far} must be available for its parent cluster. For instance, one of the far-field clusters P_{far} might have a subtree structure (shown in Fig. 4). On the leaf clusters of this subtree, the multipole moment expansions in eq. (44) are first performed, where the expansion centre $\mathbf{r}_{\text{c}}$ is the centre point of the axis-parallel cuboid which entirely encloses the triangles in each leaf cluster. Then, the M2M transformations given by eq. (52) are performed upward along this sub-tree (red arrows in Fig. 4, see also Section A.3) with the new expansion centre $\mathbf{r}_{\acute{c}}$ being the centre of their parents. This upward procedure is terminated up until to the cell of P_{far}. After that, the computed far-field integral over P_{far} centred at $\mathbf{r}_{\acute{c}}$ is then shifted onto the centre of the parent of τ (τ_p), $\acute{\mathbf{r}}_{\text{c}}$, in terms of the M2L transformation by eq. (58). Now, the local expansion coefficients $\mathbf{L}_{\text{I}}^{nm}$ and $\mathbf{L}_{\text{II}}^{nm}$ at $\acute{\mathbf{r}}_{\text{c}}$ are available. To obtain the local expansion coefficients at the centre of τ, $\acute{\mathbf{r}}_{\acute{c}}$, the L2L transformations are applied by eq. (61). Furthermore, since the clusters contained in P_{inter} are also far away from τ, using a similar procedure, the far-field integrals over P_{inter} centred at $\mathbf{r}_{\acute{c}}$ could be shifted onto the centre of τ, $\acute{\mathbf{r}}_{\acute{c}}$, in terms of the M2L transformation by eq. (58). Here, the far-field integrals are directly transformed onto the centre of τ, not to the centre of its parent τ_p, therefore $\acute{\mathbf{r}}_{\acute{c}}$ replaces $\acute{\mathbf{r}}_{\text{c}}$ in eq. (58). As discussed in Section A.2, there are no shared triangles among P_{far}, P_{near} and P_{inter}. Triangles among

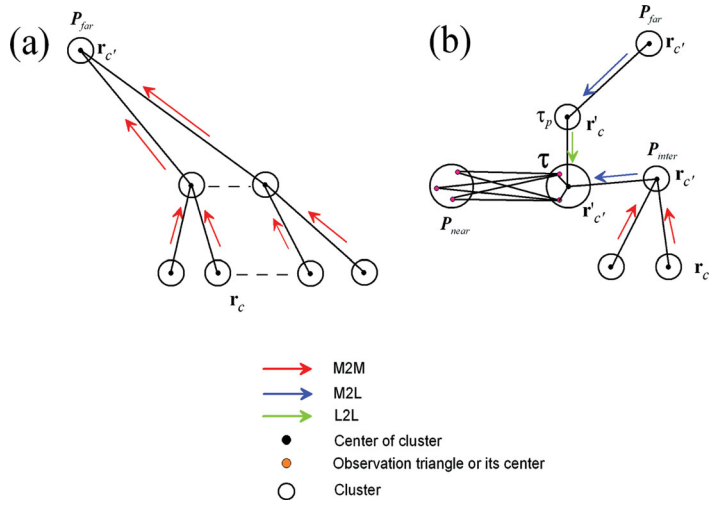

Figure 4. (a) Illustration of M2M transformations on a cluster tree. (b) Illustration of surface integration for a cluster τ in terms of M2L and L2L transformations. The cluster τ_p is the parent cluster of cluster τ. The far-field and interaction-field and near-field clusters of τ are identified with Algorithm 2.

P_{far}, P_{near} and P_{inter} completely cover the air–Earth interface Γ, that is

$$P_{\text{far}} \bigcap P_{\text{inter}} = \varnothing, \tag{62}$$

$$P_{\text{inter}} \bigcap P_{\text{near}} = \varnothing, \tag{63}$$

$$P_{\text{near}} \bigcap P_{\text{far}} = \varnothing, \tag{64}$$

$$P_{\text{far}} \bigcup P_{\text{near}} \bigcup P_{\text{inter}} = \Gamma. \tag{65}$$

Then, all the far-field integrals over $P_{\text{far}} + P_{\text{inter}}$ with respect to each observation triangle (with $\acute{\mathbf{r}}$ being its centroid) in τ could be computed as (using eq. 59)

$$\mathbf{A}_{\text{far}}\mathbf{X}(\acute{\mathbf{r}}) = \sum_{n=0}^{p}\sum_{m=-n}^{n}\begin{pmatrix}\mathbf{R}_{\text{I}}^{nm}(\acute{\mathbf{r}}-\acute{\mathbf{r}}_{\acute{c}})\,.\,[\mathbf{L}_{\text{I}}^{nm}(\acute{\mathbf{r}}_{\acute{c}})]^T \\ \mathbf{R}_{\text{II}}^{nm}(\acute{\mathbf{r}}-\acute{\mathbf{r}}_{\acute{c}})\,.\,[\mathbf{L}_{\text{II}}^{nm}(\acute{\mathbf{r}}_{\acute{c}})]^T\end{pmatrix}, \quad |\acute{\mathbf{r}}-\acute{\mathbf{r}}_{\acute{c}}| < |\mathbf{r}-\acute{\mathbf{r}}_{\acute{c}}|, \tag{66}$$

where

$$\mathbf{L}_{\text{I}}^{nm}(\acute{\mathbf{r}}_{\acute{c}}) = \underbrace{\mathbf{L}_{\text{I}}^{nm}(\acute{\mathbf{r}}_{\acute{c}}, \acute{\mathbf{r}}_{\acute{c}} \xrightarrow{L2L} \acute{\mathbf{r}}_{\acute{c}})}_{P_{\text{far}}} + \underbrace{\mathbf{L}_{\text{I}}^{nm}(\acute{\mathbf{r}}_{\acute{c}}, \mathbf{r}_{\acute{c}} \xrightarrow{M2L} \acute{\mathbf{r}}_{\acute{c}})}_{P_{\text{inter}}}, \tag{67}$$

$$\mathbf{L}_{\text{II}}^{nm}(\acute{\mathbf{r}}_{\acute{c}}) = \underbrace{\mathbf{L}_{\text{II}}^{nm}(\acute{\mathbf{r}}_{\acute{c}}, \acute{\mathbf{r}}_{\acute{c}} \xrightarrow{L2L} \acute{\mathbf{r}}_{\acute{c}})}_{P_{\text{far}}} + \underbrace{\mathbf{L}_{\text{II}}^{nm}(\acute{\mathbf{r}}_{\acute{c}}, \mathbf{r}_{\acute{c}} \xrightarrow{M2L} \acute{\mathbf{r}}_{\acute{c}})}_{P_{\text{inter}}}. \tag{68}$$

The near-field integrals over P_{near} must be directly evaluated using the singular integral techniques (Ylä-Oijala & Taskinen 2003; Ren *et al.* 2010). Once the multipole moments are computed on the cluster tree, the number of operations required to evaluate the above local expansion coefficients $\mathbf{L}_{\text{I}}^{nm}(\acute{\mathbf{r}}_{\acute{c}})$ and $\mathbf{L}_{\text{II}}^{nm}(\acute{\mathbf{r}}_{\acute{c}})$ is about $O(\log m)$ (Hackbusch & Nowak 1989). Therefore, the time complexity for the AMFM-BEM approach is reduced to

$$F = O(m \log m) \tag{69}$$

for each iteration. The reader is referred to Gumerov & Duraiswami (2004a) for a detailed time complexity analysis. Incorporating these three transformations, the multilevel fast multipole method reduces the computational time and memory cost significantly. Further details of the implementation of this algorithm are provided in Appendix A.

IMPEDANCES AND VERTICAL MAGNETIC TRANSFER FUNCTIONS

Once the system of linear eqs (37) is solved by the standard BEM procedure or the system (38) is solved by the AMFM-BEM algorithm, the electric field $\mathbf{E}$ (V m^{-1}) and magnetic field $\mathbf{H} = \frac{1}{\mu}\mathbf{B}$ (A m^{-1}) on the common surface Γ are computed in terms of surface currents and

surface charges. Assuming that there is a local coordinate system (u, v, n) at each measuring site, the components of the electric fields and magnetic fields are related by an impedance tensor **Z** and the vertical magnetic transfer function (VMT) **T** (Berdichevsky & Dmitriev 2008). To compute the impedance matrix **Z** and the VMT **T**, two sets of electromagnetic fields (on the Earth side of the interface) for both the E_x^p and H_x^p polarizations are needed. The impedance tensor is determined as follows:

$$\begin{bmatrix} Z_{uu} & Z_{uv} \\ Z_{vu} & Z_{vv} \end{bmatrix} = \begin{bmatrix} E_u^{E_x^p} & E_u^{H_x^p} \\ E_v^{E_x^p} & E_v^{H_x^p} \end{bmatrix} \begin{bmatrix} H_u^{E_x^p} & H_u^{H_x^p} \\ H_v^{E_x^p} & H_v^{H_x^p} \end{bmatrix}^{-1}. \tag{70}$$

The VMT is computed from the expression

$$\begin{bmatrix} T_u \\ T_v \end{bmatrix} = \begin{bmatrix} H_u^{E_x^p} & H_v^{E_x^p} \\ H_u^{H_x^p} & H_v^{H_x^p} \end{bmatrix}^{-1} \begin{bmatrix} H_n^{E_x^p} \\ H_n^{H_x^p} \end{bmatrix}. \tag{71}$$

Note that in eqs (70) and (71) the use of superscripts H_x^p and E_x^p on the **E** and **H** components in local co-ordinates (E_u, E_v) and (H_u, H_v) denotes that the primary (p) incident magnetic field **H** or the electric field **E** is polarized in the x direction. For 1-D and 2-D models which are invariant along the strike or the x direction, H_x^p would be referred to as the TM mode and E_x^p would be referred to as the TE mode. In our examples, we only consider the effect of one angle of incidence, that is inclination, and disregard the azimuthal angle of incidence. Furthermore, in our 3-D examples, we consider only vertical incidence along the z-axis and receivers located on a topographical axis of symmetry. In this special situation, the above definitions of an impedance tensor with four elements and a VMT with two elements are still reasonable to approximate a 3×3 impedance tensor for the full 3-D case. It should be noted that at sufficiently high frequency the Earth transmission angle deviates from the normal for oblique incidence in air. In this case, the more general definition of the impedance tensor with nine elements, that establish the transfer functions between all three components of the electric and magnetic fields, would have to be employed. Furthermore, three source polarizations would be necessary to define this impedance tensor (Berdichevsky & Dmitriev 2008).

Once the impedance tensor is available, the apparent resistivities and phases are extracted from the basic definitions

$$\rho_a^{ij} = \frac{1}{\omega\mu_0}|Z_{ij}|^2, \; i, j = u, v, \tag{72}$$

$$\phi^{ij} = \arctan\left[Im(Z_{ij})/Re(Z_{ij})\right]. \tag{73}$$

NUMERICAL EXAMPLES

To perform the numerical experiments, the resistivity of free air is set to $\rho_0 = \frac{1}{\sigma_0} = 10^{16}\,\Omega$m . The boundary conditions enforced on the surfaces Γ_0 and Γ_1 are the analytical solutions of 1-D half-space models, which assume that Γ_0 and Γ_1 should be far enough away (such as 5–10 skin depths) from the topographic surface. The amplitude of the incident E_x^p polarized field or H_x^p polarized field for these analytical solutions is arbitrarily set to unit value at the air–Earth interface ($z = 0$). In the numerical solution, similar unit values are assumed for the magnitude of the field value in the x-direction (H_x^p or E_x^p) of the incident wave. The plane wave can have an arbitrary angle of incidence.

Benchmark 1: half-space model

A half-space model is first used to verify our numerical solutions against analytical solutions. The resistivity of the homogeneous Earth is 10 000 Ωm . The magnetic permeability of the Earth is the same as that of free space, that is, $\mu_1 = \mu_0 = 4\pi \times 10^{-7}$ Vs Am^{-1}; the dielectric permittivity of the Earth is chosen as $\varepsilon_1 = 5\varepsilon_0$ to be in the typical range of plutonic rocks as, for instance, granite, where $\varepsilon_0 = 8.854 \times 10^{-12}$ F m^{-1} is the free space value.

First, we consider plane waves vertically incident on the air–Earth interface at frequencies from $f = 0.001$ Hz to 300 kHz. The standard BEM approach is used. All computations use the same mesh with 13 nodes and 16 triangles. The computational domain is $[-6\,\text{km}, 6\,\text{km}]^2$, and the computational time for each case is less than 1 s, and the memory cost is less than 10.0 MB. Solutions of our BEM approach shown in Fig. 5 are comparable to the analytical 1-D solutions (Ward & Hohmann 1987). The absolute values of the relative errors for the apparent resistivities are less than 0.01 per cent and the absolute phase errors are less than 0.002°. It is obvious that for a highly resistive subsurface, as considered here, displacement currents play an important role at the RMT frequency range ($f = 10$–300 kHz). Over this frequency range, both the apparent resistivities and the phases decrease with increasing frequency. In the MT low frequency range $f = 0.001$ Hz to 1 kHz, both apparent resistivities and phases converge to their quasi-static theoretical values of 10, 000 Ωm and 45°, respectively, because conduction currents are dominant.

Next, we vary the angle of incidence for the plane wave impinging on the air–Earth interface. For this wave we assume that the electric field E_x^p is polarized in the x-direction, with the magnetic field polarized in the y–z plane of propagation (TE-mode). Three separate angles of inclination are investigated, $\Psi = 0°, 30°, 90°$ (measured w.r.t. z-axis), for frequencies from $f = 10$ to 300 kHz. The standard BEM approach is used. All computations use the same mesh with 760 nodes and 1425 triangles. The computational domain is $[-300\,\text{m}, 300\,\text{m}]^2$, and the computational time for each case is about 180.0 s, and the memory cost is about 1.6 GB. Fig. 6 shows the numerical solutions for this E_x^p

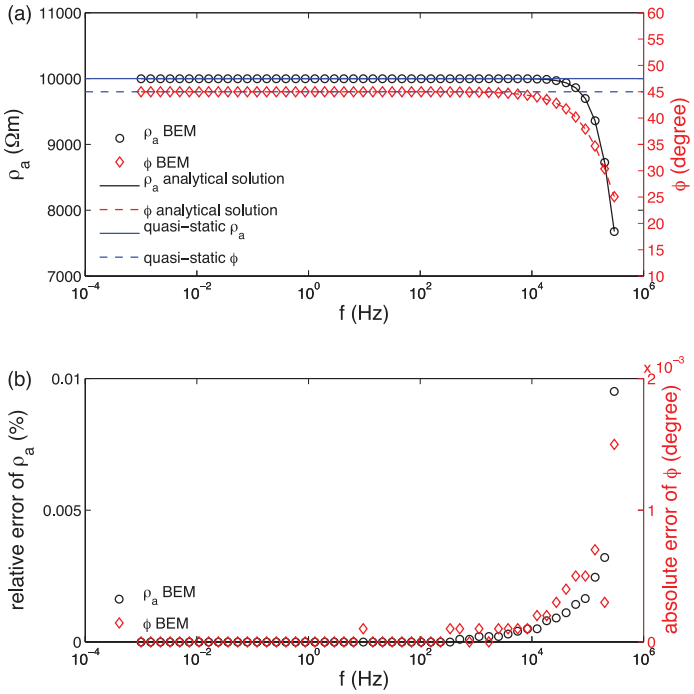

Figure 5. (a) Apparent resistivities ρ_a and phases ϕ on a homogeneous half-space with a resistivity of 10000 Ωm and a relative dielectric permittivity of 5.0 at frequencies of $f = 0.001$ Hz to 300 kHz and at normal incidence, that is, at an angle of incidence $\Psi = 0^\circ$ (Benchmark 1 example). (b) Deviations of our BEM solutions from the analytical 1-D solutions from Ward & Hohmann (1987).

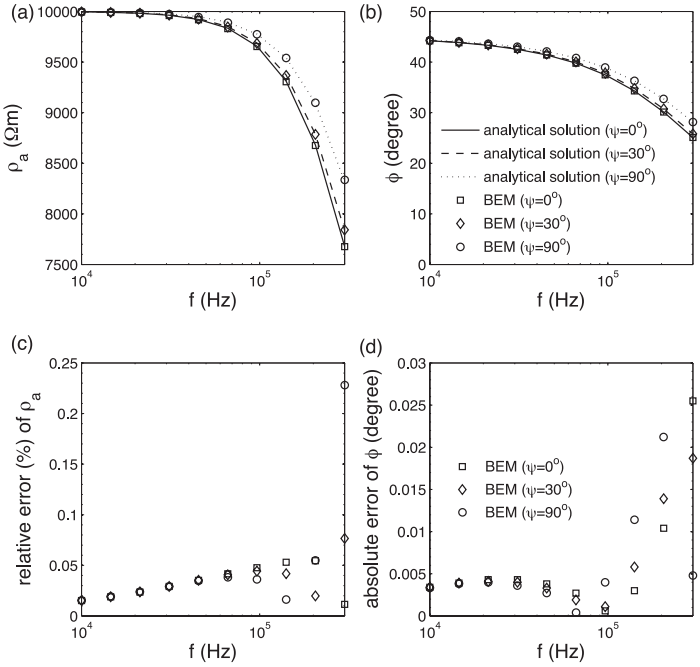

Figure 6. Apparent resistivities ρ_a (a) and phases ϕ (b) of the TE-mode on a homogeneous half-space with a resistivity of 10 000 Ωm and a relative dielectric permittivity of 5.0 at frequencies of $f = 10$ to 300 kHz for three angles of incidence $\Psi = 0^\circ$, 30°, 90° (Benchmark 1 example). Panels (c) and (d) show deviations of our BEM solutions from the analytical 1-D solutions (Ward & Hohmann 1987).

polarization case obtained from the new BEM approach, and the corresponding analytical 1-D solutions (Ward & Hohmann 1987). The relative errors of the apparent resistivities are less than 0.25 per cent and the phase errors are less than 0.03°, for all three incidence angles. The apparent resistivities and phases decrease smoothly with increasing frequency, reaching values of 7678 Ωm and 25.1°, respectively, at 300 kHz, for the vertical incidence case. Due to Snell's law, with an increasing incidence angle Ψ (away from the vertical) the horizontal wavenumber gets larger and the vertical wavenumber gets smaller, causing the apparent resistivities and phases for $\Psi = 90^\circ$ and 30° to be

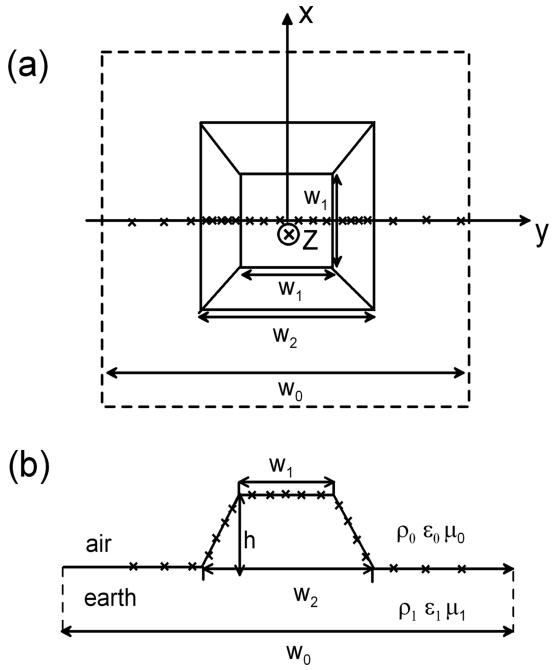

Figure 7. Geometry of the trapezoidal hill models [(a) top-view and (b) cross-section] in the Cartesian (x, y, z) coordinate system. The size of the hilltop square is $w_1 \times w_1$, and that of the base square is $w_2 \times w_2$, with h being the height of the hill. A geometrical approximation is made to reduce the infinite air–Earth interface to a finite square of size $w_0 \times w_0$. The resistivity of the free space is ρ_0, ε_0 is the free space dielectric permittivity, and μ_0 is the free space magnetic permeability; ρ_1, ε_1 and μ_1 are the corresponding electromagnetic parameters for the Earth. Receiver positions are indicated by black crosses.

Table 1. Parameters of the trapezoidal hill model.

	w_0 (km)	w_1 (m)	w_2 (m)	h (m)	ρ_1 (Ωm)	$\varepsilon_1/\varepsilon_0$	μ_1/μ_0	f(Hz)
Model I	40	450	2000	450	100	1	1	2
Model II	4	45	200	45	3×10^4	5	1	3×10^5

larger than the values for $\Psi = 0^\circ$. The percentage deviation between the curves is minimal at $f = 10$ kHz and reaches its maximum value of about 10 per cent at $f = 300$ kHz.

Benchmark 2: trapezoidal hill model I

The trapezoidal hill model I shown in Fig. 7 and Table 1 was chosen to compare the numerical solutions obtained from our standard BEM approach and our new AMFM-BEM approach against those from the independent 3-D edge-based FEM (Nam *et al.* 2007). The same geometry for the hill is adopted as was used in the model of Nam *et al.* (2007). The size of the hilltop square is 450 × 450 m, the size of the square base is 2000 × 2000 m, and the height of this hill is 450 m. A geometrical approximation is made to cut off the horizontally infinite air–Earth interface into a finite square of size 40 × 40 km. The resistivity of the Earth is $\rho_1 (= 1/\sigma_1) = 10^2$ Ωm; the dielectric permittivity of the Earth is ε_0 and the magnetic permeability is μ_0.

The trapezoidal hill surface is discretized into 298 nodes and 565 triangles. Hence, 3390 complex-valued unknowns are distributed over the surface. Side lengths of the triangles near the trapezoidal hill are less than 10 per cent of the skin depth at the considered frequency of 2 Hz and the longest side length is about 1.0 skin depth. At this frequency and medium conductivity the electromagnetic field diffuses into the Earth vertically at a speed of about $10^{-4}c$, where c is the speed of light. The fields are measured right beneath the air–Earth interface. In addition to the solutions of the standard surface integral equations obtained by direct solvers, the solutions of the AMFM-BEM computed with GMRES solvers (Balay *et al.* 2010) are also presented in Fig. 8. The results displayed are for the profile along the y-axis as shown in Fig. 7(a). Apparent resistivities and phases for both the xy-component (Figs 8 b and d) and the yx-component (Figs 8 a and c) of the impedance tensor are given for each algorithm, whereas the magnetic transfer functions T_x (Fig. 8e) and T_y (Fig. 8f) are given only for the standard BEM approach, because the AMFM approach yields the same patterns. The two numerical solutions are in close agreement. Furthermore, they are verified by the reference solutions which were redrawn from the edge-based FEM solutions of Nam *et al.* (2007), also presented in Fig. 8. Away from the hill on the flat topography, the apparent resistivity approaches the true value of the Earth resistivity of 100 Ωm, while the phase reaches its homogeneous flat earth model value of 45°. Over the top of the hill the apparent resistivity ρ_a^{xy} drops appreciably by a factor of 2 whereas ρ_a^{yx} shows an oscillatory pattern, with higher values on the flanks and lower values beneath the hill top. This overall drop in apparent resistivity for positions above the hill is due to the decrease in current density associated with such topography. A valley type structure would produce the opposite effect, concentrating the current lines and increasing the apparent resistivity (Jiracek 1990). The cusps on the ρ_a^{yx} plot

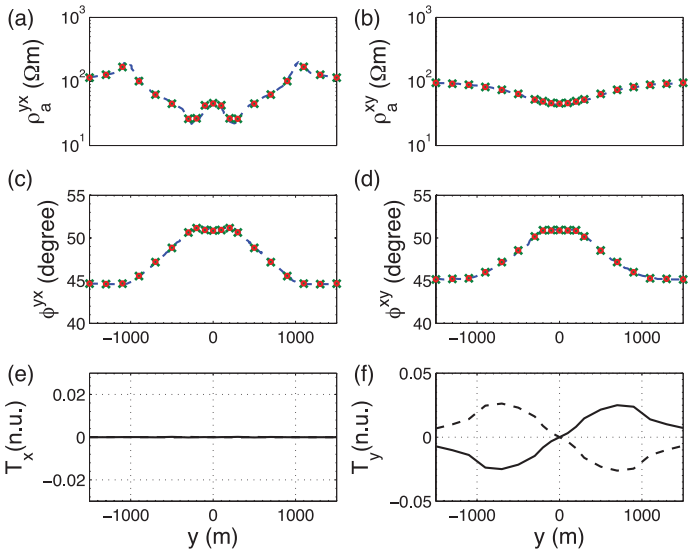

Figure 8. Numerical results for apparent resistivities [(a) and (b)) and phases ((c) and (d)] of the off-diagonal impedance tensor elements as well as the VMTs T_x and T_y [(e) and (f)] for the trapezoidal hill model I. Numerical solutions of the apparent resistivities and phases from our standard BEM method (green crosses) and our AMFM-BEM approach (red circles) are in good agreement with the solutions for a 3-D edge-based FEM code (Nam *et al.* 2007, dashed blue lines) using structured meshes, where the green crosses are overlapping with red circles. As in Nam *et al.* (2007), the modelling results are given w.r.t. a global Cartesian co-ordinate system. Because of the similarity of patterns of VMTs from the standard BEM method and the AMFM-approach, we only plot results of VMTs from the standard BEM algorithm, with the real components shown by solid curves and the imaginary components shown by the dashed curves.

Table 2. Comparison of memory and time costs of the standard BEM algorithm and the AMFM-BEM method on the trapezoidal hill model I. For the AMFM-BEM method, the number of expansion terms is 6, the maximum number of triangles in the leaf cluster is 50 and the admissibility condition is 2.5.

	BEM		AMFM-BEM	
Memory (MB)	737.3		196.6	
Time (s)	93.1		131.0	
	For right-hand side vectors **Y**	71.1	For right-hand side vectors **Y**	71.1
	For system matrix **A**	10.3	Set up cluster tree	0.1
	For solver MUMPS	11.7	Banded matrix $\mathbf{A}_{\text{near}}$	5.1
			Pre-compute multipole moments	5.8
			For solver GMRES in 18 iterations	48.9

occur at changes in slope of the surface topography. The phase in both cases increases by about 5° above the hill. Note the symmetry of the patterns which is due to the profile being taken across the centre of the structure and an angle of incidence of 0°. The T_x component of the VMT is zero in accordance with theory because of the symmetry of the body and the orientation of the profile. The T_y component is zero at the very top of the hill and approaches zero well away from the sloping sides but changes sign as the hill is crossed.

Compared to the large number of unknowns used in the FEM solutions (Nam *et al.* 2007), our new BEM approach needs less unknowns. In both standard BEM and AMFM-BEM methods, errors only arise from the surface mesh discretization. Numerical errors from a volume discretization of the air and Earth domains are avoided. Therefore, our surface integral approach may provide more accurate results than the FEM methods (Nam *et al.* 2007). As shown in Table 2, the computation time of the standard BEM approach is about 93.1 s (two source polarizations are considered). It is 131 s for the AMFM-BEM approach on a PC with Intel(R) Xeon(TM) CPU 3.20 GHz and RAM 8.0 GB. About 71.1 s are spent on computing the right-hand side vectors for both BEM and AMFM-BEM methods. The time complexity of computing the right hand side vector is $O(mn)$, where m is the number of triangles on the air–Earth interface Γ and n is the number of triangles on Γ_0 and Γ_1. In this experiment, we only applied the fast multipole concept on the air–Earth interface. Therefore, if the fast multipole method was applied to the evaluation of right-hand side vectors, the total computational time would be dramatically reduced.

In addition, this example shows that our standard BEM approach and AMFM-BEM approaches can provide model responses (apparent resistivities and phases) that are in good agreement with the quasi-static FEM computations at low frequency. Shown in Table 2, the memory cost for the standard BEM is about 737.3 MB, whereas it is only 196.6 MB for the AMFM-BEM method. It should be noted that for this small scale model under consideration, the standard BEM method is faster than the fast multipole accelerated BEM approach (see Table 2). The reason is that the cost of pre-computation of expansion coefficients and the cost of M2M and M2L and L2L transformations is much higher than the cost of direct integrations since the number of triangles is sufficiently small. However, with increasing model size, the standard BEM becomes increasingly expensive in terms of speed and memory cost and reaches a point where it can no longer be used. This will be illustrated in the next example.

Table 3. Numbers of *M2M*, *M2L* and *L2L* transformations performed at each level on the cluster tree for the trapezoidal hill model-II and total execution times for all three transformations. The cluster tree contained 2515 clusters and 1895 leaf clusters at 9 levels. The above transformations required 257 seconds at each iteration of the GMRES solver. The GMRES solver stopped after less than 30 iterations for both E_x^p and H_x^p polarizations, with a relative tolerance of 10^{-5}. About 94 per cent of the computational time was spent by the M2L transformations at each iteration. This implies that faster M2L transformations are needed to further improve the efficiency of our AMFM algorithm. The total memory cost of our AMFM approach was about 700 MB.

Level of cluster tree	*M2M* (upward pass)	*M2L* (downward pass)	*L2L* (downward pass)
2	64	124	0
3	256	1436	64
4	1024	7804	256
5	96	35 516	1024
6	276	2472	96
7	695	9684	276
8	83	21 616	695
9	0	1281	83
Total	2494	79 933	2494
Time (s)	7.45	85.10	7.45

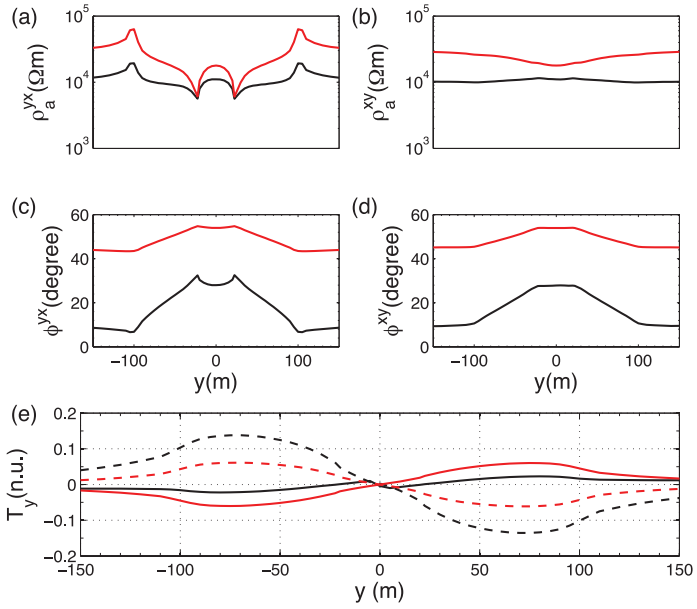

Figure 9. Comparison of apparent resistivities ρ_a and phases ϕ and VMT T_y for the trapezoidal hill model II for two cases, with (black curves) and without (red curves) displacement currents, at $f = 300$ kHz. The solid curves stand for the real components of the VMT T_y and the dashed curves are for the imaginary components.

Effects of displacement currents

We now turn our attention to the effects of displacement currents on a scaled-down version of the trapezoidal hill model (shown in Fig. 7 and Table 1) but still involving significant topography (dip variations of about 30°). Here we use a much higher frequency than in the previous section, that is, $f = 300$ kHz, and a much higher Earth resistivity, that is, $\rho = 30$ kΩm. The hill surface is discretized into 4324 nodes and 8487 triangles. Consequently, 50 922 complex-valued unknowns are distributed over the surface. The side length of the triangles near the trapezoidal hill is less than 0.1 skin depth and the longest side length far away from the hill is about 1.0 skin depth. Due to this dense surface mesh, the standard BEM approach cannot solve this problem on a personal computer. The total memory requirement for the standard BEM approach is about 38.6 GB, which exceeds the capacity of a typical personal computer. For larger models with sizes of half a million unknowns the total memory cost would approach about 3800 GB, which would even exceed the capacity of a modern computer cluster. In contrast, the AMFM-BEM approach required only about 0.7 GB of computer memory (see Table 3 for detailed run-time parameters), and for a large model with half a million unknowns approximately 7 GB computer memory would be occupied. Since both resistivity and frequency are much higher than in the low frequency Benchmark 2 example, displacement currents are highly relevant in this example.

In Fig. 9, we compare the apparent resistivities, phases and VMTs along the y profile over the centre of the hill (Fig. 7 a) for two cases: allowing for displacement currents, and the quasi-static approximation in which displacements currents are ignored. For such a situation the displacement currents ought to be about half as strong as the conduction currents and the speed of the EM disturbance in the rock about 0.86c.

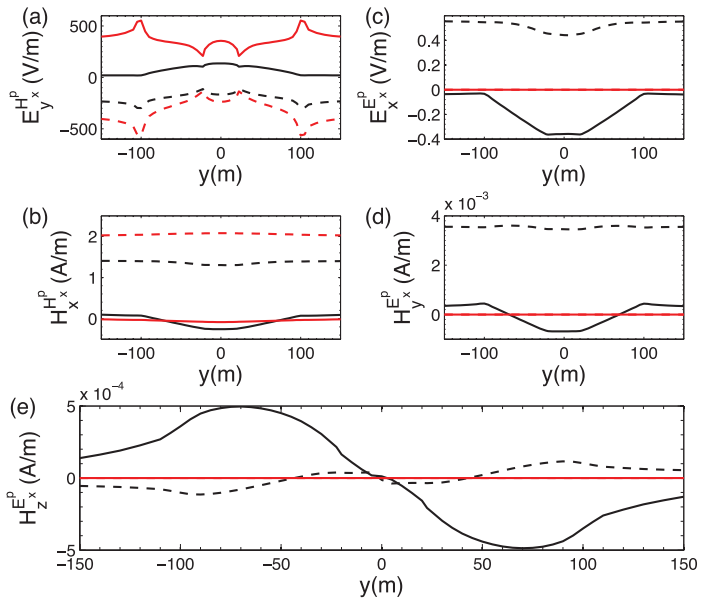

Figure 10. Comparison of horizontal x and y components of the **E** and **H** fields and vertical z component of the **H** field on the Earth side of the topography for a profile along the y-axis for the trapezoidal hill model II. Results shown are for cases with (black curves) and without (red curves) displacement currents, for the two incident polarizations E_x^p and H_x^p. The dashed and solid curves stand for the real and imaginary components of the electromagnetic fields, respectively.

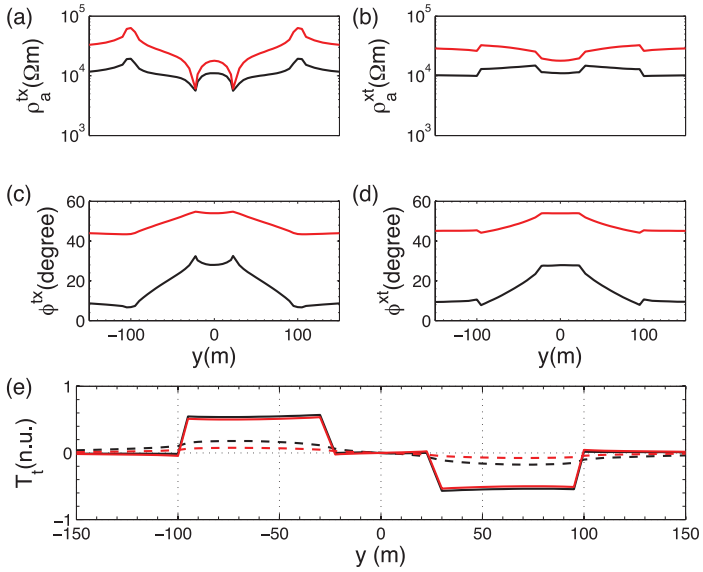

Figure 11. Apparent resistivities ρ_a, phases ϕ, and VMT T_t for the trapezoidal hill model II, where electromagnetic responses are computed in the local coordinate system, in which t is the direction along the profile, and n is the normal to the topographic surface. Black curves are for the case with displacement currents and red curves are for the quasi-static case (without displacement currents). The solid curves stand for the real components of the VMT T_t and the dashed curves are for its imaginary components.

The results for apparent resistivity and phase of the *yx*-component of the impedance tensor are presented in Figs 9(a) and (c), respectively, whereas the corresponding results for the *xy*-component of the impedance tensor are plotted in Figs 9(b) and (d). For the VMT, only the y component is shown (Fig. 9e). For Z_{yx}, we once again find cuspidal effects at breaks in surface topography on the apparent resistivity and phase plots, but the effect is more pronounced than in the previous example. The changes in slope are more subdued for Z_{xy}. Due to the high frequency and Earth resistivity in this example, the effect of displacement currents is strong, not just in phase (Figs 9c and d) but also in apparent resistivity and T_y (Figs 9 a, b and e). The behaviour of the different components of the electromagnetic field along the profile is shown in Fig. 10 for further insight and clarification.

In actual MT and RMT field surveying, the electromagnetic responses are normally measured in a local coordinate system (x, t, n) along the profile, with the 'vertical' component in the direction normal (n) to the topography and the radial component (t) along the profile in the tangential direction. Component x is horizontal and perpendicular to the profile direction. Therefore, we wish to present the apparent resistivities, phases and VMTs (Fig. 11) in the local coordinate system along the profile. The fields computed in the y and z directions are

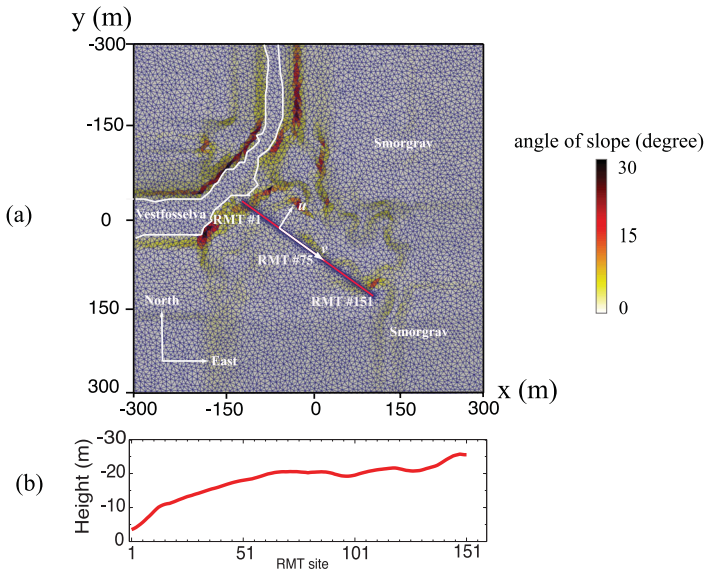

Figure 12. (a) A local view of the central part of the surface mesh for the Smørgrav RMT field example (after Kalscheuer *et al.* 2012) in a global (x, y, z) coordinate system. Triangles are colour coded according to the angle of the slope of the topography as measured against the zenith. The maximum angle of slope is 28.9°. A local (u, v, n) coordinate system is introduced on measuring sites, where u and v directions are perpendicular and parallel to the receiver line, respectively, and the direction of n is normal to the air–Earth interface pointing into the Earth. A total of 151 computational sites are located along the profile (in red) at 2.46 m intervals. (b) The topographic variations along the profile, observe the rapid increase in topographic height at the southeast end of the profile.

Table 4. Mesh and execution parameters for the Norway field example, T_t is the total time cost for the M2M, M2L and L2L translations in each iteration. The number of expansion terms $p = 10$ is used to guarantee more accurate results (increasing T_t). The maximum number of triangles in the leaf cluster is 20 and the admissibility condition is $\gamma = 2.0$.

Case	Frequency (Hz)	#Model	Domain (km^2)	#Triangles	#Unknowns	Iterations	T_t (s)	Memory (GB)
	2×10^3	1	$[-2, 2]^2$	15 414	92 484	36	700.5	4.8
$\rho = 30\ \Omega$m	2×10^4	2	$[-1, 1]^2$	8087	48 522	47	577.0	3.6
	2.26×10^5	3	$[-1, 1]^2$	14 851	89 106	137	588.0	4.6
	2×10^3	4	$[-5, 5]^2$	15 458	92 748	18	758.5	5.0
$\rho = 3000\ \Omega$m	2×10^4	5	$[-2, 2]^2$	15 414	92 484	21	698.5	4.8
	2.26×10^5	6	$[-2, 2]^2$	15 414	92 484	53	701.0	4.8

transformed to the new values in the t and n local reference directions by rotation factors ($\cos\theta$, $\sin\theta$) where θ is the angle of the slope. In terms of these rotation factors, the approximate shapes of the slopes are directly reflected in the patterns, as shown for the trapezoidal hill model in Fig. 11.

The numerical examples presented in the above two sections clearly illustrate the pronounced effects of topography on MT responses and also the strong effects of displacements currents in RMT surveying.

Smørgrav field example

Last, we applied our newly developed algorithms to study the topographic effect for a RMT field example of the Smørgrav site which is located about 65 km southwest of Oslo in southern Norway (Kalscheuer *et al.* 2012). The inversion algorithm utilized by Kalscheuer *et al.* (2012) assumes a flat air–Earth interface. Assuming two resistivity values of 30 and 3000 Ωm as they are typically encountered at Smørgrav, we assess the topographic effect of the measured field responses and provide guidelines for data editing to mitigate topographic effect on the inverse models of Kalscheuer *et al.* (2012). As shown in Fig. 12(a), RMT fields are simulated at 151 RMT sites (marked in red) at 2.46 m spacing. Fig. 12(b) depicts the topographic variations along the profile. The starting site close to the Vestfosselva river is marked as RMT #1 and the last site close to Smørgrav is marked as RMT #151. The actual field profile starts at RMT #4 and ends at RMT #135; and the actual station spacing employed in the field was 10 m. Derived from Fig. 12(a), the maximum angle of slope is 28.9°. The slopes close to the starting sites (nearby the Vestfosselva river) and the ending sites and the middle sites are rather steep. The calculations are carried out in a local (u, v, n) coordinate system (Fig. 12 a), where u and v are perpendicular and parallel to the receiver line, respectively. The direction of n is normal to the air–Earth interface pointing into the Earth.

Three frequencies, 2.0×10^3, 2.0×10^4 and 2.26×10^5 Hz, are tested. Two values of the resistivity for the homogeneous Earth, 30 and 3000 Ωm, are used. The mesh and execution parameters of these six examples are listed in Table 4. A local mesh section of the example with a frequency of 2.0×10^3 Hz and a 30 Ωm Earth is shown in Fig. 12.

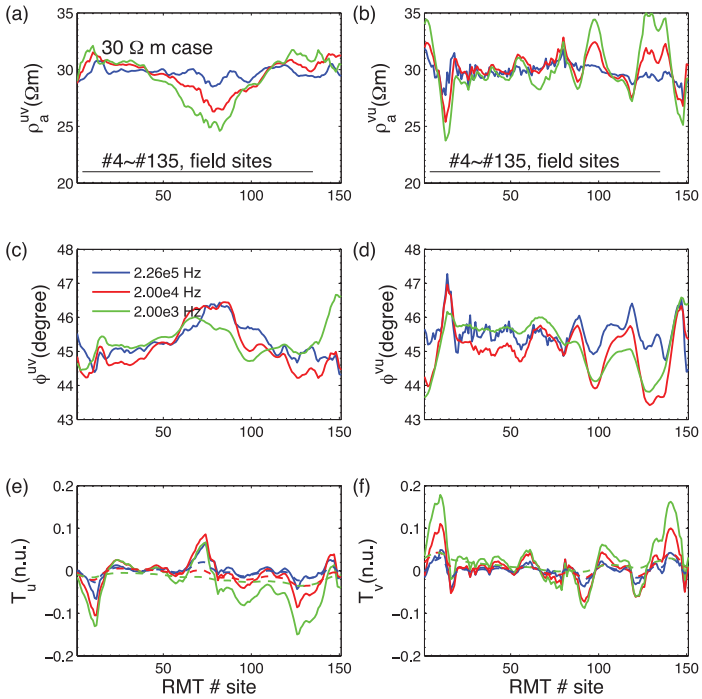

Figure 13. Apparent resistivities ρ_a and phases ϕ of impedances Z_{uv} and Z_{vu} and VMTs T_u and T_v of the Smørgrav model. The resistivity of the Earth is 30 Ωm. The solid and dashed curves stand for the real and imaginary components of the VMTs, respectively.

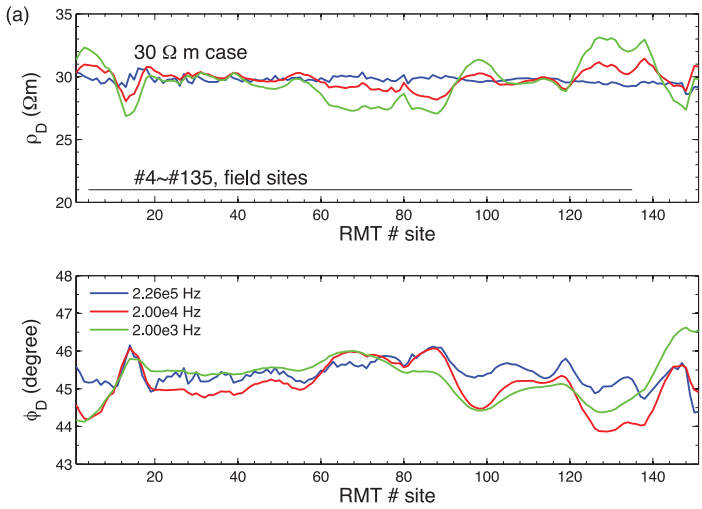

Figure 14. Apparent resistivities ρ_D and phases ϕ_D of the determinant impedance Z_D of the Smørgrav model. The resistivity of the Earth is 30 Ωm.

The apparent resistivities and phases of Z_{uv} and Z_{vu} and the VMTs T_u and T_v for a 30 Ωm Earth are shown in Fig. 13. In the 30 Ωm case, the maximum mismatches (deviations from data calculated for flat topography) due to the topographic effect on the apparent resistivies (Fig. 13) are about 6.0 Ωm (∼20.0 per cent), which occur at the middle and end sites. The maximum mismatches for the phases (Fig. 13) are about 2°. The apparent resistivities and phases of the determinant impedance $Z_D = \sqrt{Z_{uu}Z_{vv} - Z_{uv}Z_{vu}}$ are shown in Fig. 14. As to be expected from calculations of Pedersen & Engels (2005), the apparent resistivies and phases of Z_D (Fig. 14) are less sensitive to the topographic effects, where the maximum mismatches for apparent resistivies and phases reduce to less than 10.0 per cent and 1.5°, respectively. This suggests the use of Z_D data in the RMT inversion (Kalscheuer *et al.* 2012) and furthermore, it could be beneficial to remove or downweight the field RMT data around the middle of the profile (sites at #75) and the start and endpoints of the profile (at sites #12 and #124, respectively). Similar results of the determinant impedance for the case of a 3000 Ωm Earth are shown in Fig. 15. Here, the relative deviations of the apparent resistivities (up to 26.7 per cent) and absolute deviations in phases (up to 2.0°) are much more pronounced than for a 30 Ωm Earth. These deviations exceed typical measurement errors of 5 per cent and 1.43°. Hence, to mitigate topographic effects in inverse models constructed under the assumption of a flat air–Earth interface, it is advisable to assume error floors of 26.7 per cent and 2.0° for apparent resistivities and phases on resistive ground of about 3000 Ωm. Furthermore, the small-scale variations evident in Figs 13–15 suggest that the site spacing of 10 m should be refined.

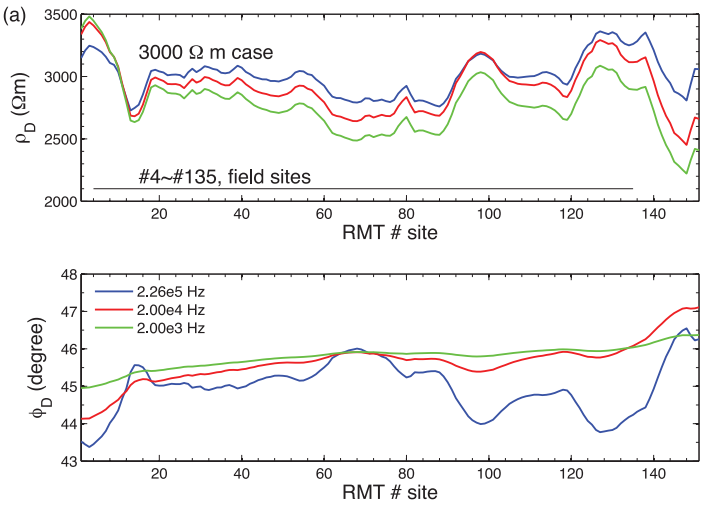

Figure 15. Apparent resistivities ρ_D and phases ϕ_D of the impedance Z_D of the Smørgrav model. The resistivity of the Earth is 3000 Ωm.

As indicated by the iteration numbers of model #5 and model #6, that share the same mesh (see Table 4), the condition numbers of the system matrix increase with increasing frequency. In our experience, when the sizes of triangles which are far away from the central topographic surface are quite different from those of the central topographic region, iteration numbers of the GMRES solver increase dramatically. The entries in the system matrix are computed in the form of surface integrals over triangles. If triangle sizes are large, then the entries arising from these large triangles will be dominant. Therefore, grids with gradually increasing triangle sizes would lead to large condition numbers. To solve this problem, it is better to refine these areas outside the main region with topographic undulations while keeping the computational domain on an reasonable scale.

CONCLUSIONS

We developed a generalized surface integral formula for wide-band 3-D electromagnetic problems. It was successfully applied to solve 3-D plane-wave electromagnetic induction problems. Such an approach is the most attractive and suitable option for pure topographical problems from the accuracy point of view, because it avoids the need for volume discretization of the air and Earth domain. However, unlike the FEM method, it cannot easily deal with complex geometrical models such as arbitrary conductivity distributions underground. The 2-D surface discretization not only leads to an easy implementation of mesh triangulation but also reduces the number of unknowns. To derive this novel surface integral formula, which avoids the instability problems at low frequency for 3-D electromagnetic modelling (Zhao & Chew 2000), the full set of four boundary conditions is employed simultaneously such that the requirement of vanishing current flow out of the Earth into the air is satisfied at low frequency. In addition, a rescaling technique is employed for both the MFIE and EFIE to have the same order of magnitude. This avoids the generation of an ill-conditioned system of linear equations.

The standard BEM, which could be used to solve this surface integral formula quickly exceeds the memory capacity of modern computers for problems involving hundreds of thousands of unknowns. To make our surface integral formula capable of dealing with large-scale 3-D geo-electromagnetic problems, a novel optimal and simplified matrix-free adaptive multilevel fast multipole BEM has been developed and implemented. In co-operation with iterative solvers such as the GMRES technique, this matrix-free AMFM algorithm only needs an $O(m \log m)$ time complexity to compute the multiplication of the system of linear equations and an initial solution vector and a $O(m)$ memory cost to store all expansion coefficients and basis functions.

Comparisons of our BEM results against the FEM results of Nam *et al.* (2007) for a trapezoidal hill model at a frequency of 2 Hz (MT range) and the analytical solutions for a half-space model over the frequency range 0.001 Hz to 300 kHz (Ward & Hohmann 1987) confirm the validity and applicability of our new BEM algorithm to low frequency problems. For highly resistive environments, our numerical results confirm that displacement currents can have similar strength to the conductive currents in the RMT frequency rage. Under such conditions, electromagnetic fields, impedance tensor elements and vertical magnetic transfer functions are strongly affected, compared with solutions under the quasi-static assumption. Therefore, it can become critical that computed RMT responses incorporate the effects of displacements currents to avoid false interpretation of RMT data.

As demonstrated for the Smørgrav field example, the determinant impedance is less sensitive to topographic effects, than the impedance tensor and the vertical magnetic transfer function. At many sites, the errors caused by topographic effects are in the range of the measuring errors, which implies the validity of a 2-D inversion approach under the assumption of a flat air–Earth interface. For sites with topographic errors of the size of or larger than the measuring errors, an increase of data errors or data removal have to be performed *prior to* 2-D inversion to reduce topographic effects on inverse models.

It should be emphasized that the purpose of this study is not only to develop a code to accurately compute the electromagnetic responses for 3-D steep topographical problems at both MT and RMT frequency ranges, but also to act as the first step to eliminate the volume

discretization of the air domain with the help of the surface integral formula. The elimination of the air space becomes critical for high frequency RMT applications, because a nearly globally dense mesh is required to discretize the air space for the FEM and FDM methods. This not only increases the computational cost but also leads to large numerical errors arising from the improper discretization of the air space. Although the implementation of the presented surface integral formula is limited to the two connected bodies case (which is a pure topographical problem only involving the air space and the homogeneous Earth), it is still possible to apply the surface integral formula to solve problems with anomalous bodies embedded in the homogeneous Earth. In this case, the surface integral formula needs to be individually applied in each anomalous body with constant electrical parameters. However this will increase the implementation complexity of the surface integral approach. Therefore, to deal with complex models, the next step in our research is to develop a hybrid modelling scheme integrating the surface integral approach described here for the air space with an unstructured mesh FEM solver to compute the subsurface responses in highly complex environments. Besides the capability of solving for responses of complex models, this hybrid approach is expected to be more accurate than the FEM and FDM methods due to the absence of numerical errors arising from a volume discretization of the air space, especially at high frequencies.

Although only numerical examples of plane-wave electromagnetic problems are tested, our presented surface integral formula is applicable to controlled-source problems. For the controlled-source case, a volume integral term accounting for the spatial source would have to be added into the surface integral formula.

ACKNOWLEDGMENTS

This work was performed in ETH's Applied and Environmental Geophysics Group headed by Prof. Dr. Alan Green, who made it possible to conduct the study. This research was financially supported by the China Scholarship Council Foundation (2008637007), ETH Zurich and the National Natural Science Foundation of China (40874072).

REFERENCES

Abramowitz, M. & Stegun, I., 1964. *Handbook of Mathematical Functions with Formulas, Graphs, and Mathematical Tables,* Dover publications, New York.

Ahmed, M., Lavers, J. & Burke, P., 1988. A comparision of boundary integral formulations for 3D axisymmetric eddy-current problems, *IEEE Trans. Magn.,* **24,** 138–141.

Amestoy, P., Duff, I., L'Excellent, J. & Koster, J., 2002. A fully asynchronous multifrontal solver using distributed dynamic scheduling, *SIAM J. Matrix Anal. Appl.,* **23,** 15–41.

Amos, D., 1986. Algorithm 644: a portable package for Bessel functions of a complex argument and nonnegative order, *ACM Trans. Math. Softw.,* **12,** 265–273.

Aprea, C., Booker, J. & Smith, J., 1997. The forward problem of electromagnetic induction: accurate finite-difference approximations for two-dimensional discrete boundaries with arbitrary geometry, *Geophys. J. Int.,* **129,** 29–40.

Avdeev, D., Kuvshinov, A., Pankratov, O. & Newman, G., 2002. Three-dimensional induction logging problems, Part I: an integral equation solution and model comparisons, *Geophysics,* **67,** 413–426.

Badea, E., Everett, M., Newman, G. & Biro, O., 2001. Finite-element analysis of controlled-source electromagnetic induction using Coulomb-gauged potentials, *Geophysics,* **66,** 786–799.

Balay, S. *et al.*, 2010. *PETSc Users Manual, Tech. rep., Argonne National Laboratory*.

Bapat, M. & Liu, Y., 2010. A new adaptive algorithm for the fast multipole boundary element method, *Comput. Model. Eng. Sci.,* **58,** 161–184.

Berdichevsky, M.N. & Dmitriev, V.I., 2008. *Models and Methods of Magnetotellurics,* Springer, Berlin and Heidelberg.

Bleszynski, E., Bleszynski, M. & Jaroszewicz, T., 1996. Aim: adaptive integral method for solving large-scale electromagnetic scattering and radiation problems, *Radio Sci.,* **31,** 1225–1252.

Blome, M., Maurer, H.R. & Schmidt, K., 2009. Advances in three-dimensional geoelectric forward solver techniques, *Geophys. J. Int.,* **176,** 740–752.

Borup, D. & Gandhi, O., 1984. Fast-Fourier-transform method for calculation of SAR distributions in finely discretized inhomogeneous models of biological bodies, *IEEE Trans. Microw. Theory Tech.,* **32,** 355–360.

Buchau, A., Huber, C., Rieger, W. & Rucker, W., 2000. Fast BEM computations with the adaptive multilevel fast multipole method, *IEEE Trans. Magn.,* **36,** 680–684.

Çakır, Ö., 2006. The multilevel fast multipole method for forward modelling the multiply scattered seismic surface waves, *Geophys. J. Int.,* **167**(2), 663–678.

Çakır, Ö., 2009. Forward modelling the multiply scattered 2.5-D teleseismic P waves accelerated by the multilevel fast multipole method, *Geophys. J. Int.,* **176**(2), 505–517.

Candansayar, M.E. & Tezkan, B., 2008. Two-dimensional joint inversion of radiomagnetotelluric and direct current resistivity data, *Geophys. Prospect.,* **56,** 737–749.

Colton, D. & Kress, R., 1983. *Integral Equation Methods in Scattering Theory,* John Wiley & Sons, New York.

Doherty, J., 1988. EM modelling using surface integral equations, *Geophys. Prospect.,* **36,** 644–668.

Epton, M. & Dembart, B., 1995. Multipole translation theory for the 3-dimensional Laplace and Helmholtz equations, *SIAM J. Sci. Comput.,* **16,** 865–897.

Franke, A., Börner, R.-U. & Spitzer, K., 2007. Adaptive unstructured grid finite element simulation of two-dimensional magnetotelluric fields for arbitrary surface and seafloor topography, *Geophys. J. Int.,* **171,** 71–86.

Fujiwara, H., 2000. The fast multipole method for solving integral equations of three-dimensional topography and basin problems, *Geophys. J. Int.,* **140**(1), 198–210.

Galassi, M., Gough, B., Jungman, G., Theiler, J., Davies, J., Booth, M. & Rossi, F., 2009. *GNU Scientific Library Reference Manual,* Network Theory Ltd., United Kingdom.

Gumerov, N. & Duraiswami, R., 2004a. *Fast Multipole Methods for the Helmholtz Equation in Three Dimensions,* Elsevier Science, Amsterdam.

Gumerov, N. & Duraiswami, R., 2004b. Recursions for the computation of multipole translation and rotation coefficients for the 3-D Helmholtz equation, *SIAM J. Sci. Comput.,* **25,** 1344–1381.

Haber, E., Ascher, U., Aruliah, D. & Oldenburg, D., 2000. Fast simulation of 3D electromagnetic problems using potentials, *J. Comput. Phys.,* **163,** 150–171.

Hackbusch, W. & Nowak, Z., 1989. On the fast matrix multiplication in the boundary element method by panel clustering, *Numer. Math.,* **54,** 463–491.

Harrington, R., 1993. *Field Computation by Moment Methods,* Wiley-IEEE Press, New York.

Hohmann, G., 1975. Three-dimensional induced polarization and electromagnetic modeling, *Geophysics,* **40,** 309–324.

Homentcovschi, D., 2002. Minimum-order regular boundary integral equations for three-dimensional eddy-current problem, *IEEE Trans. Magn.,* **38,** 3433–3438.

Hou, J., Mallan, R.K. & Torres-Verdin, C., 2006. Finite-difference simulation of borehole EM measurements in 3D anisotropic media using coupled scalar-vector potentials, *Geophysics,* **71,** G225–G233.

Ismail, N. & Pedersen, L., 2011. The electrical conductivity distribution of the Hallandsas Horst, Sweden: a controlled source radiomagnetotelluric study, *Near Surf. Geophys.,* **9,** 45–54.

Jin, J., 2002. *The Finite Element Method in Electromagnetics,* Wiley-IEEE Press, New York.

Jiracek, G., 1990. Near-surface and topographic distortions in electromagnetic induction, *Surv. Geophys.,* **11**(2), 163–203.

Kalscheuer, T., Bastani, M., Donohue, S., Persson, L., Pfaffhuber, A.A., Reiser, F. & Ren, Z., 2012. Delineation of a quick clay structure at Smørgrav, Norway, with electromagnetic methods, *J. appl. Geophys.,* in revision.

Kalscheuer, T., Pedersen, L.B. & Siripunvaraporn, W., 2008. Radiomagnetotelluric two-dimensional forward and inverse modelling accounting for displacement currents, *Geophys. J. Int.,* **175,** 486–514.

Kalscheuer, T., Juanatey, G., Meqbel, N. & Pedersen, L.B., 2010. Non-linear model error and resolution properties from two-dimensional single and joint inversions of direct current resistivity and radiomagnetotelluric data, *Geophys. J. Int.,* **182,** 1174–1188.

Key, K. & Weiss, C., 2006. Adaptive finite-element modeling using unstructured grids: the 2D magnetotelluric example, *Geophysics,* **71,** G291–G299.

Lee, J., Zhang, J. & Lu, C., 2004. Sparse inverse preconditioning of multilevel fast multipole algorithm for hybrid integral equations in electromagnetics, *IEEE Trans. Antennas Propag.,* **52,** 2277–2287.

Li, Y. & Key, K., 2007. 2D marine controlled-source electromagnetic modeling, Part 1: an adaptive finite-element algorithm, *Geophysics,* **72,** WA51–WA62.

Liu, E. & Lamontagne, Y., 1998. Geophysical application of a new surface integral equation method for EM modeling, *Geophysics,* **63,** 411–423.

Liu, G. & Becker, A., 1992. Evaluation of terrain effects in AEM surveys using the boundary element method, *Geophysics,* **57,** 272–278.

Liu, Y., 2009. *Fast Multipole Boundary Element Method—Theory and Applications in Engineering,* Cambridge University Press, Cambridge.

Mackie, R., Smith, J. & Madden, T., 1994. 3D electromagnetic modeling using finite-difference equations- the magnetotelluric example, *Radio Sci.,* **29,** 923–935.

May, D. & Knepley, M., 2011. Optimal, scalable forward models for computing gravity anomalies, *Geophys. J. Int.,* **187,** 161–177.

Mayergoyz, I., 1982. Boundary integral equation of minimum order for the calculation of three-dimensional eddy current problems, *IEEE Trans. Magn.,* **18,** 536–539.

Mitsuhata, Y. & Uchida, T., 2004. 3D magnetotelluric modeling using the T-Omega finite-element method, *Geophysics,* **69,** 108–119.

Mukherjee, S. & Everett, M.E., 2011. 3D controlled-source electromagnetic edge-based finite element modeling of conductive and permeable heterogeneities, *Geophysics,* **76,** F215–F226.

Nam, M., Kim, H., Song, Y., Lee, T., Son, J. & Suh, J., 2007. 3D magnetotelluric modelling including surface topography, *Geophys. Prospect.,* **55,** 277–287.

Newman, G. & Alumbaugh, D., 2002. Three-dimensional induction logging problems, Part 2: a finite-difference solution, *Geophysics,* **67,** 484–491.

Operto, S., Virieux, J., Amestoy, P., L'Excellent, J.-Y., Giraud, L. & Ali, H. B.H., 2007. 3d finite-difference frequency-domain modeling of visco-acoustic wave propagation using a massively parallel direct solver: a feasibility study, *Geophysics,* **72**(5), SM195–SM211.

Parry, J. & Ward, S., 1971. Electromagnetic scattering from cylinders of arbitrary cross section in a conductive half space, *Geophysics,* **36,** 67–100.

Pedersen, L. & Engels, M., 2005. Routine 2D inversion of magnetotelluric data using the determinant of the impedance tensor, *Geophysics,* **70,** G33–G41.

Pedersen, L., Bastani, M. & Dynesius, L., 2005. Groundwater exploration using combined controlled-source and radiomagnetotelluric techniques, *Geophysics,* **70,** G8–G15.

Pedersen, L.B., Bastani, M. & Dynesius, L., 2006. Some characteristics of the electromagnetic field from radio transmitters in Europe, *Geophysics,* **71,** G279–G284.

Pérez-Gavilán, J. & Aliabadi, M., 2001. Symmetric Galerkin BEM for multiconnected bodies, *Commun. Numer. Methods Eng.,* **17,** 761–770.

Pusch, D. & Ostrowski, J., 2010. Robust FEM/BEM coupling for magnetostatics on multiconnected domains, *IEEE Trans. Magn.,* **46,** 3177–3180.

Ren, Z., Kalscheuer, T. & Maurer, H., 2010. Accurate and robust evaluation of singular boundary element integrals for computing 3D radiomagnetotelluric fields, in *Proceedings of the Expanded Abstracts EAGE Near Surface Meeting Zurich,* EAGE, Switzerland.

Rokhlin, V., 1992. *Diagonal forms of translation operators for Helmholtz equation in three dimensions, Tech. rep., DTIC Document*.

Rucker, W., Hoschek, R. & Richter, K., 1995. Various BEM formulations for calculating eddy currents in terms of field variables, *IEEE Trans. Magn.,* **31,** 1336–1341.

Seher, T. & Tezkan, B., 2007. Radiomagnetotelluric and Direct Current Resistivity measurements for the characterization of conducting soils, *J. appl. Geophys.,* **63,** 35–45.

Shen, J., 1995. *Computational Electromagnetics Using Boundary Elements: Advances in Modelling Eddy Currents,* Computational Mechanics Publications, Southampton.

Shewchuk, J., 1996. Triangle: engineering a 2D quality mesh generator and Delaunay triangulator, *Lecture Notes Comput. Sci.,* **1148,** 203–222.

Streich, R., 2009. 3D finite-difference frequency-domain modeling of controlled-source electromagnetic data: direct solution and optimization for high accuracy, *Geophysics,* **74**(5), F95–F105.

Taskinen, M. & Ylä-Oijala, P., 2006. Current and charge integral equation formulation, *IEEE Trans. Antennas Propag.,* **54,** 58–67.

Tezkan, B. & Saraev, A., 2008. A new broadband radiomagnetotelluric instrument: applications to near surface investigations, *Near Surf. Geophys.,* **6,** 245–252.

Tezkan, B., Goldman, M., Greinwald, S., Hördt, A., Müller, I., Neubauer, F. & Zacher, G., 1996. A joint application of radiomagnetotellurics and transient electromagnetics to the investigation of a waste deposit in Cologne (Germany), *J. appl. Geophys.,* **34,** 199–212.

Tezkan, B., Georgescu, P. & Fauzi, U., 2005. A radiomagnetotelluric survey on an oil-contaminated area near the Brazi Refinery, Romania, *Geophys. Prospect.,* **53,** 311–323.

Tsuboi, H. & Misaki, T., 1987. Three-dimensional analysis of eddy-current distributions by the boundary element method using vector variables, *IEEE Trans. Magn.,* **23,** 3044–3046.

Ward, S. & Hohmann, G., 1987. Electromagnetic theory for geophysical applications: electromagnetic methods in applied geophysics, *Tulsa: Soc. Explor. Geophys., Nabighian MN (Ed.),* **1,** 131–311.

Weidelt, P., 1975. Electromagnetic induction in three-dimensional structures, *J. Geophys.,* **41,** 85–109.

Xu, S., Ruan, B., Zhou, H., Chen, L. & Xu, S., 1997. Numerical modeling of 3-D terrain effect on MT field, *Sci. China Ser. D-Earth Sci.,* **40,** 269–275.

Ylä-Oijala, P., 2008. Numerical analysis of combined field integral equation formulations for electromagnetic scattering by dielectric and composite objects, *Prog. Electromag. Res.,* **3,** 19–43.

Ylä-Oijala, P. & Taskinen, M., 2003. Calculation of CFIE impedance matrix elements with RWG and n x RWG functions, *IEEE Trans. Antennas Propag.,* **51,** 1837–1846.

Ylä-Oijala, P. & Taskinen, M., 2007. Improving conditioning of electromagnetic surface integral equations using normalized field quantities, *IEEE Trans. Antennas Propag.,* **55,** 178–185.

Zhao, J. & Chew, W., 2000. Integral equation solution of Maxwell's equations from zero frequency to microwave frequencies, *IEEE Trans. Antennas Propag.,* **48**(10), 1635–1645.

Zhdanov, M.S., Lee, S.K. & Yoshioka, K., 2006. Integral equation method for 3D modeling of electromagnetic fields in complex structures with inhomogeneous background conductivity, *Geophysics,* **71,** G333–G345.

Zheng, D., 1997. Three-dimensional eddy current analysis by the boundary element method, *IEEE Trans. Magn.,* **33,** 1354–1357.

Algorithm 1 : Construction of a cluster tree (Γ, $l_{\max}$, $n_{\max}$, Υ). Given Γ, $l_{\max}$ and $n_{\max}$, find Υ.

Step 1: $l = 0$, form root cluster τ_0^0. Find a minimal axis-parallel cuboid C_0^0 enclosing the surface Γ, $\tau_0^0 = \sum \triangle_i \in C_0^0$;

Step 2: $l = 1$, form a set of child clusters τ_k^1 of τ_0^0, with indices $0 \leq k \leq 7$. Subdivide C_0^0 into eight subcuboids C_k^1, delete empty cuboids;

Step 3: $l = l + 1$, $l \leq l_{\max}$, find a set of clusters τ_k^l. For all clusters τ_k^{l-1} of level $l - 1$, if τ_k^{l-1} is not identified as a leaf cluster (numbers of triangles in τ_k^{l-1} is less than or equal to $n_{\max}$), then find the child clusters of τ_k^{l-1} by the subdivision approach used in Step 2. Thus, a set of clusters τ_k^l for level l is obtained. If all clusters in τ_k^l are leaf clusters (numbers of triangles in τ_k^l are less than or equal to $n_{\max}$), go to Step 4; else go to Step 3;

Step 4: Eventually, the cluster tree Υ has the form of $\Upsilon = \sum_{l=0}^{lmax} \sum_k \tau_k^l$. Stop.

APPENDIX A: DETAILS ON THE ADAPTIVE MULTILEVEL FAST MULTIPOLE ALGORITHM

A1 Construction of a cluster tree

The common surface Γ is divided into a set of disjoint triangles $\Gamma = \sum_{i=0}^{N-1} \triangle_i$. The sizes of the triangles are non-uniformly distributed with a small size around the regions of interest. To deal with this non-uniform triangulation, a cluster tree is adaptively constructed. In the cluster tree Υ, each cell contains a cluster. A cluster τ is a union of several triangles $\tau = \triangle_1 \cup \triangle_2 \cup \cdots \cup \triangle_{n^\tau}$, where n^τ is the number of triangles enclosed in the cluster τ. The deepest level of this cluster tree is $l_{\max}$, the level for the root cluster is 0, and τ_k^l denotes the kth cluster (or cell) at the level l of Υ. At level l, we assume a total of n_l clusters to exist so that the surface Γ is a union of n_l clusters, that is, $\Gamma = \tau_1^l \cup \tau_2^l \cup \cdots \cup \tau_{n_l}^l$. For a cluster to be identified as a leaf cluster (i.e. a cluster that is not allowed to be further divided into child clusters), the number of triangles enclosed is required to be less than or equal to a predefined maximum number $n_{\max}$. Assuming L_k^l is the kth leaf cluster at level l, the summation of all leaf clusters from all levels also forms a complete cover of the surface Γ, that is, for $\sum_{l=0}^{lmax} \sum_{k=1}^{n_l^L} L_k^l = \Gamma$, where n_l^L is the total number of leaf clusters at level l.

At the level $l = 0$ of the cluster tree Υ, the root cluster τ_0^0 contains a complete set of all triangles pertaining to Γ, which are confined by a minimal axis-parallel cuboid that entirely encloses the surface Γ. To find the clusters at level $l = 1$ of the cluster tree Υ, the entire cuboid is then subdivided in eight small cuboids, by dividing the side lengths of the original cuboid by a factor of 2. Hence, all eight cuboids share the midpoint of the original cuboid as a common point. Each small cuboid enclosing a cluster τ_k^1. Possibly, some of these small cuboids do not contain any part of the surface Γ. These empty cuboids must be deleted so that the number of clusters τ_k^1 at the level $l = 1$ of Υ is less than or equal to 8. The subdivision is then performed on all clusters of level $l = 1$ to generate a set of child clusters which are located at the next level. This iterative procedure is terminated when the number of triangles in these child clusters approaches a maximum permissible number of triangles $n_{\max}$ or the number of the next level equals a maximum level number $l_{\max}$. Unlike the recursive tree generating algorithm given in Blome *et al.* (2009) and Hackbusch & Nowak (1989), a loop-based algorithm is designed for simplified implementation which is described in Algorithm (1).

A2 Identification of near-field, far-field and interaction-field clusters

Given a cluster τ, we need to find its optimal sets of near-field clusters P_{near}, far-field clusters P_{far} and interaction-field clusters P_{inter}. For the root cluster τ_0^0, $P_{\text{near}}(\tau_0^0) = \tau_0^0$, $P_{\text{far}}(\tau_0^0) = \emptyset$, $P_{\text{inter}}(\tau_0^0) = \emptyset$. For clusters τ_k^1 at level $l = 1$, $P_{\text{near}}(\tau_k^1) = \tau_k^1$, $P_{\text{far}}(\tau_k^1) = \emptyset$, $P_{\text{inter}}(\tau_k^1) = \emptyset$. Observe that all clusters τ_k^1 are classified as near-field clusters, because their confining cuboids share the midpoint of the cuboids of τ_0^0 as a common point. For each cluster τ_k^l at level $l_{\max} \geq l \geq 2$, we first obtain its parent far-field clusters $P_{\text{far}}(\tau_k^{l-1})$ and near-field clusters $P_{\text{near}}(\tau_k^{l-1})$; then the far-field clusters for τ_k^l are its parent far-field clusters, $P_{\text{far}}(\tau_k^l) = P_{\text{far}}(\tau_k^{l-1})$, because any cluster that is far away from the parent cluster must be far away from the child clusters. In its parent's near-field clusters $P_{\text{near}}(\tau_k^{l-1})$, some clusters might be the far-field cluster with respect to τ_k^l. Here, an admissible factor γ is introduced to identify the far-field relationship between two clusters (Hackbusch & Nowak 1989), shown in Fig. 3

$$\frac{D(\tau_i, \tau_j)}{\max\left[R(\tau_i), R(\tau_j)\right]} \geq \gamma, \tag{A1}$$

where $D(\tau_i, \tau_j)$ is the distance between two clusters τ_i and τ_j, and $R(\tau_i)$ is the diameter of cluster τ_i. If a cluster in $P_{\text{near}}(\tau_k^{l-1})$ satisfies the admissibility condition given in eq. (A1) with respect to τ_k^l, this cluster is put into the interaction field clusters $P_{\text{inter}}(\tau_k^l)$ of τ_k^l. The remaining clusters in $P_{\text{near}}(\tau_k^{l-1})$ are classified into $P_{\text{near}}(\tau_k^l)$.

It is valuable to point out that for any cluster τ, the combination of its far-field, and near-field, and interaction clusters forms a complete coverage of all triangles of the whole cluster tree Υ. Here, for a cluster at level $l \geq 2$, the number of near-field clusters is kept to an optimal minimum value compared to others approaches (Bapat & Liu 2010), and its admissible far-field and interaction-field clusters are fully identified. For the purpose of an easy implementation, this simple and optimal procedure is described in Algorithm (2).

Algorithm 2 : Identify (Υ, γ, $P_{\rm far}$, $P_{\rm near}$, $P_{\rm inter}$). Given Υ and γ, find $P_{\rm far}$, $P_{\rm near}$, $P_{\rm inter}$ for all clusters in Υ

Step 1: $l = 0$, $P_{\rm near}(\tau_0^0) = \tau_0^0$, $P_{\rm far}(\tau_0^0) = \emptyset$, $P_{\rm inter}(\tau_0^0) = \emptyset$;

Step 2: $l = 1$, for each cluster τ_k^1 , $0 \le k \le 7$, $P_{\rm near}(\tau_k^1) = \tau_k^1$, $P_{\rm far}(\tau_k^1) = \emptyset$, $P_{\rm inter}(\tau_k^1) = \emptyset$;

Step 3: $l = 2$, $l \le l_{\rm max}$, for each cluster τ_k^l, $P_{\rm near}(\tau_k^l) = \chi$, $P_{\rm inter}(\tau_k^l) = P_{\rm near}(\tau_k^{l-1}) - \chi$, $P_{\rm far}(\tau_k^l) = P_{\rm far}(\tau_k^{l-1})$, $P_{\rm near}(\tau_k^{l-1})$ is the near-field clusters of cluster τ_k^l's parent, $P_{\rm far}(\tau_k^{l-1})$ is the far-field clusters of cluster τ_k^1's parent, χ is a set of clusters of $P_{\rm near}(\tau_k^{l-1})$ not satisfying the admissibility condition in eq. (A1);

Step 4: Stop.

A3 Upward pass, downward pass

Upward pass: for a given initial set of distributions of surface currents and charges, the upward pass algorithm (Liu 2009) is used to compute all the multipole moments $\mathbf{M}_{\rm I}^{nm}$ and $\mathbf{M}_{\rm II}^{nm}$ in eq. (44) for each cluster with level $l \ge 2$ on the cluster tree. Starting from the deepest level $l = l_{\rm max}$ on which all clusters must be leaf clusters, the direct evaluation of multipole moments centred at the geometrical centre of these leaf clusters is performed. Then, we move to the clusters at the level $l = l_{\rm max} - 1$. If one of these clusters is a leaf cluster, the direct evaluation of multipole moments is applied, otherwise we search for its child clusters. From the multipole moments of these child clusters, the multipole moments of their parent clusters at level $l = l_{\rm max} - 1$ are computed by the M2M transformation in eq. (52). This upward pass procedure is performed recursively to clusters on level $l = 2$.

Downward pass: starting from a cluster τ at level $l = 2$, we obtain its far-field and interaction field lists from Algorithm (2). If the interaction field list is not empty, the local expansion coefficients $\mathbf{L}_{\rm I}^{nm}$ and $\mathbf{L}_{\rm II}^{nm}$ of τ in eq. (54) are computed by the multipole moments of clusters in its interaction field list in terms of the M2L transformation. If the far-field list is not empty, then we should request the parent of cluster τ for the parent's local expansion coefficients which must be already computed according to this algorithm. Hence, in terms of the L2L transformation in eq. (61), the local expansion coefficients of cluster τ computed from the far-field list are available. Adding these two local expansion coefficients, the total local expansion coefficients for cluster τ are obtained. This downward pass procedure is performed recursively to clusters on level $l_{\rm max}$ and to each leaf cluster.

A4 Convergence rates of the GMRES solver

Looping over each leaf cluster, the multiplication of its local expansion coefficients and its local expansion basis functions plus the contributions from the banded sparse matrix $\mathbf{A}_{\rm near}$, successively form $\mathbf{Y}_t$, where t means the tth iteration of the generalized minimal residual (GMRES) solver. The time complexity of the AMFM method is proportional to the number of iterations ($t \le n_{it}$) used by the GMRES solver. It is well known that the convergence rate of the GMRES solver might be accelerated with some pre-conditioners. However, we use the non pre-conditioned GMRES solver in our AMFM-BEM algorithm, because our system of linear equations is well-conditioned.

Eigenvalue spectrum analysis and a comparison between the convergence rates of the GMRES solver and the Jacobian-GMRES solver for two examples are shown in Fig. A1. In Fig. A1, we plot the absolute values of the eigenvalues and the relative residuals (difference in solutions between successive iterations) versus iteration number for the two numerical examples. The first example (diagrams a and b) is for a halfspace model (see Section 4.1) and the second example (diagrams c and d) is for a topographic hill model (see Section 4.2). In Figs A1(a) and A1(c), the eigenvalues are bounded and far-away from zero. Most singular values are distributed around the hypothetical unit value. The spectral condition number estimated in terms of the SVD decomposition is less than 3 and 100 in cases (a) and (c), respectively. For the half-space model (Fig. A1b), the relative residual behaviour is presented for the GMRES and the preconditioned GMRES solver with Jacobian pre-conditioners (Balay *et al.* 2010), for both E_x^p and H_x^p polarizations. Both solvers converge rapidly to a small relative error of 10^{-10} after six iterations. For the topographical hill model (Fig. A1d), since the condition number is larger than that for the half-space model, the GMRES and Jacobian-GMRES solvers converge more slowly, requiring 18 iterations to achieve relative errors of 10^{-5}. More importantly, these results show that due to the well-conditioned surface integral formulae presented in eqs (23) and (24), there is no critical requirement to apply the pre-conditioner techniques to accelerate the iterative GMRES algorithms. Such desirable behaviour further implies that we can simply use the original GMRES solver, in co-operation with the adaptive multilevel fast multipole method, to avoid the increased complexity of implementation involved in specific pre-conditioning techniques (Lee *et al.* 2004).

APPENDIX B: EVALUATION OF MOMENT INTEGRALS

For clarity, we rewrite the moment integrals in eqs (47) and (48) over a triangle as

$$\mathbf{M}_i^{\nabla nm}(k, \mathbf{r}_{\rm c}) = \iint_{\mathbf{r}\in\triangle_i} \nabla R_n^m(k, \mathbf{r} - \mathbf{r}_{\rm c})\, {\rm d}s \tag{B1}$$

$$M_i^{nm}(k, \mathbf{r}_{\rm c}) = \iint_{\mathbf{r}\in\triangle_i} R_n^m(k, \mathbf{r} - \mathbf{r}_{\rm c})\, {\rm d}s, \tag{B2}$$

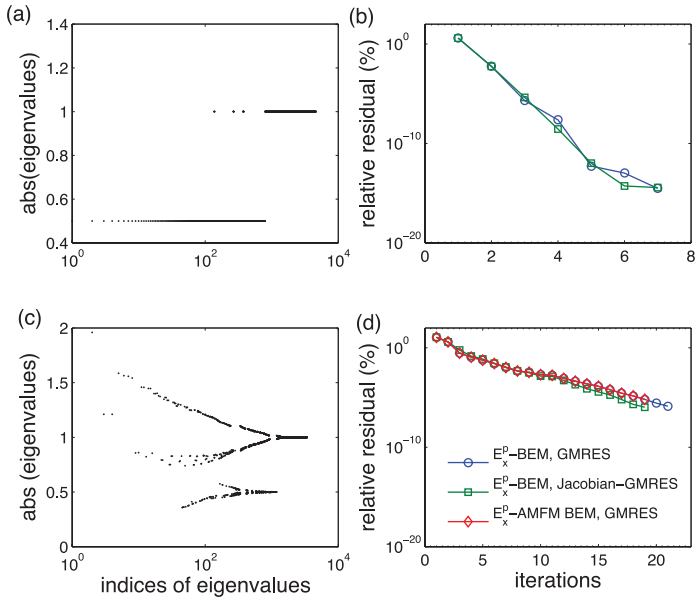

Figure A1. Eigenvalue spectral distributions of the two system matrices of sizes 4644 × 4644 and 3390 × 3390 for Benchmark 1 (a) and Benchmark 2 (c), respectively, at a frequency $f = 2$ Hz; the convergence rates of the standard BEM using both GMRES and Jacobian-GMRES solvers and the AMFM-BEM approach using the non-preconditioned GMRES algorithm, for the E_x^p polarization (similar results obtained from the H_x^p polarization are omitted here), on Benchmark 1(b) and Benchmark 2(d).

Here, R_n^m are the solid harmonics defined in the spherical coordinate system centred on the expansion point $\mathbf{r}_c$. Since there is no spherical symmetry for any triangle, we have to evaluate these moments in a global coordinate system. The coordinates of the expansion point are $\mathbf{r}_c = (x_c, y_c, z_c)$, the coordinates of a general point $\mathbf{r} \in \triangle_i$ are $\mathbf{r} = (x, y, z)$. The relationship between the global coordinates and the spherical coordinates of a point $\mathbf{r}$ is given by

$$\begin{aligned} x - x_c &= r\cos\varphi\sin\theta \qquad r \geq 0 \\ y - y_c &= r\sin\varphi\sin\theta \qquad \pi \geq \theta \geq 0 \\ z - z_c &= r\cos\theta \qquad 2\pi \geq \varphi \geq 0. \end{aligned}$$

The gradient operator ∇ on $\mathbf{r}$ is

$$\begin{pmatrix} \frac{\partial}{\partial x} \\ \frac{\partial}{\partial y} \\ \frac{\partial}{\partial z} \end{pmatrix} = \begin{pmatrix} \sin\theta\cos\varphi & \frac{1}{r}\cos\theta\cos\varphi & \frac{-1}{r}\frac{\sin\varphi}{\sin\theta} \\ \sin\theta\sin\varphi & \frac{1}{r}\cos\theta\sin\varphi & \frac{-1}{r}\frac{\cos\varphi}{\sin\theta} \\ \cos\theta & \frac{-1}{r}\sin\theta & 0 \end{pmatrix} \begin{pmatrix} \frac{\partial}{\partial r} \\ \frac{\partial}{\partial\theta} \\ \frac{\partial}{\partial\varphi} \end{pmatrix} = \mathbf{J} \begin{pmatrix} \frac{\partial}{\partial r} \\ \frac{\partial}{\partial\theta} \\ \frac{\partial}{\partial\varphi} \end{pmatrix}, \tag{B3}$$

where $\mathbf{J}$ is the Jacobian transformation matrix.

Taking into account the explicit expression for R_n^m, we have

$$\begin{aligned} \frac{\partial R_n^m}{\partial r} &= Y_n^m(\theta,\phi)\frac{\partial j_n(kr)}{\partial r} = Y_n^m(\theta,\phi)\left[\frac{n}{kr}j_n(kr) - j_{n+1}(kr)\right]k \\ \frac{\partial R_n^m}{\partial\theta} &= j_n(kr)\frac{\partial Y_n^m(\theta,\phi)}{\partial\theta} = j_n(kr)(-1)^m\sqrt{\frac{(n-|m|)!}{(n+|m|)!}}\frac{\partial P_n^{|m|}(\cos\theta)}{\partial\cos\theta}(-\sin\theta)\mathrm{e}^{\mathrm{i}m\phi} \\ \frac{\partial R_n^m}{\partial\varphi} &= \mathrm{i}m j_n(kr)Y_n^m(\theta,\phi), \end{aligned}$$

where the above spherical Bessel functions with complex arguments are evaluated by the open source AMOS library (Amos 1986).

To easily perform the numerical integrals over $\triangle_i$, a local coordinate system (ε, η, $0 \leq \varepsilon \leq 1$, $0 \leq \eta \leq 1$, $0 \leq \varepsilon + \eta \leq 1$) is introduced. In this system, a point $\mathbf{r} \in \triangle_i$ has the following definition

$$\mathbf{r} = \mathbf{r}_0(1 - \varepsilon - \eta) + \mathbf{r}_1\varepsilon + \mathbf{r}_2\eta,$$

where $\mathbf{r}_j$, $j = 0, 1, 2$ are three vertices of triangle $\triangle_i$, which should be indexed in a clock-wise or a counter-clockwise manner. Now, the moment integrals are easily evaluated as follows:

$$\mathbf{M}_i^{\nabla nm}(k, \mathbf{r}_c) = \int_0^1 \int_0^{1-\varepsilon} \mathbf{J} \begin{pmatrix} \frac{\partial R_n^m}{\partial r} \\ \frac{\partial R_n^m}{\partial \theta} \\ \frac{\partial R_n^m}{\partial \varphi} \end{pmatrix} 2\triangle \, \mathrm{d}\varepsilon \, \mathrm{d}\eta = \sum_{p=0}^{q-1} \left[\mathbf{J} \begin{pmatrix} \frac{\partial R_n^m}{\partial r} \\ \frac{\partial R_n^m}{\partial \theta} \\ \frac{\partial R_n^m}{\partial \varphi} \end{pmatrix} \right]_{(\varepsilon_p, \eta_p)} W_p \triangle, \tag{B4}$$

$$M_i^{nm}(k, \mathbf{r}_c) = \int_0^1 \int_0^{1-\varepsilon} R_n^m 2\triangle \, \mathrm{d}\varepsilon \, \mathrm{d}\eta = \sum_{p=0}^{q-1} \left[R_n^m \right]_{(\varepsilon_p, \eta_p)} W_p \triangle, \tag{B5}$$

where q is the number of Gaussian quadrature points, (ε_p, η_p) are the Gaussian quadrature points, W_p are the weights (Jin 2002), and $\triangle$ is the area of triangle $\triangle_i$ and $2\triangle$ is the determinant involved in the transformation from the global coordinate system to the local coordinate system.